Summer 2018

Cloud Microphysical Properties based on Airborne In Situ Observations and Evaluation of a Weather Forecasting Model and a Global Climate Model

John D'Alessandro
San Jose State University

Recommended Citation
D'Alessandro, John, "Cloud Microphysical Properties based on Airborne In Situ Observations and Evaluation of a Weather Forecasting Model and a Global Climate Model" (2018). *Master's Theses*. 4935.
DOI: https://doi.org/10.31979/etd.7855-fqvh
https://scholarworks.sjsu.edu/etd_theses/4935

CLOUD MICROPHYSICAL PROPERTIES BASED ON AIRBORNE IN SITU OBSERVATIONS AND EVALUATION OF A WEATHER FORECASTING MODEL AND A GLOBAL CLIMATE MODEL

A Thesis

Presented to

The Faculty of the Department of Meteorology and Climate Science

San José State University

In Partial Fulfillment

of the Requirements for the Degree

Master of Science

by

John D'Alessandro

August 2018

The Designated Thesis Committee Approves the Thesis Titled

CLOUD MICROPHYSICAL PROPERTIES BASED ON AIRBORNE IN SITU OBSERVATIONS AND EVALUATION OF A WEATHER FORECASTING MODEL AND A GLOBAL CLIMATE MODEL

by

John D'Alessandro

APPROVED FOR THE DEPARTMENT OF METEOROLOGY AND CLIMATE SCIENCE

SAN JOSÉ STATE UNIVERSITY

AUGUST 2018

Minghui Diao, Ph.D.	Department of Meteorology and Climate Science
Craig Clements, Ph.D.	Department of Meteorology and Climate Science
Neil Lareau, Ph.D.	Department of Meteorology and Climate Science

ABSTRACT

CLOUD MICROPHYSICAL PROPERTIES BASED ON AIRBORNE IN SITU OBSERVATIONS AND EVALUATION OF A WEATHER FORECASTING MODEL AND A GLOBAL CLIMATE MODEL

By John D'Alessandro

Global cloud coverage has a substantial impact on local and global radiative budgets. It is necessary to correctly represent clouds in numerical weather models to improve both weather and climate predictions. This study evaluates in situ airborne observations of cloud microphysical properties and compares results with the Weather Research and Forecasting model (WRF) and Community Atmosphere Model version 5 (CAM5). Dynamical conditions producing supersaturated conditions with respect to ice at high altitudes in regions diagnosed by convective activity are explored using observations taken from the Deep Convective Clouds and Chemistry (DC3) campaign, and results are compared with simulated data from WRF. The WRF analysis tests multiple cloud microphysics schemes and finds the model requires much stronger updrafts to initiate large magnitudes of ice supersaturation (ISS) relative to observations. This is primarily due to the microphysics schemes over-predicting ice particle number concentrations (Nc_{ice}), which rapidly deplete the available water vapor. The frequency of different cloud phases and the distribution of relative humidity (RH) over the Southern Ocean is explored using in situ airborne observations taken from the O_2/N_2 Ratio and CO_2 Airborne Southern Ocean Study (ORCAS) and compared with simulated data from CAM5. The CAM5 simulations produce comparable distributions of RH in clear-sky conditions at warmer temperatures (>-20°C). However, simulations fail to capture high frequencies of clear-sky ISS at colder temperatures (<-40°C). In addition, CAM5 underestimates the frequency of subsaturated conditions within ice phase clouds from -40°–0°C.

TABLE OF CONTENTS

LIST OF TABLES

LIST OF FIGURES

LIST OF ABBREVIATIONS

2DC	2 Dimensional Optical Array Probe
CAM5	Community Atmosphere Model version 5
CDP	Cloud Droplet Probe
CFD	Cumulative Frequency Distribution
CWC	Condensed Water Content
DC3	Deep Convective Clouds and Chemistry campaign
GFS	Global Forecast System
GV	Gulfstream V
IN	Ice Nuclei
ISS	Ice Supersaturation
IWC	Ice Water Content
LWC	Liquid Water Content
MPC	Mixed Phase Clouds
NCAR	National Center for Atmospheric Research
NSF	National Science Foundation
RH	Relative Humidity
RHi	Relative Humidity with respect to ice
RHliq	Relative Humidity with respect to liquid
Nc	Number concentration of ice
Nc_{ice}	Ice particle number concentration
Nc_{liq}	Liquid droplet number concentration
ORCAS	O_2/N_2 Ratio and CO_2 Airborne Southern Ocean campaign
PDF	Probability Density Function
SLW	Supercooled Liquid Water
VCSEL	Vertical Cavity Surface Emitting Laser
w	Vertical velocity
WBF	Wegener-Bergeron-Findeison process
WRF	Weather Research and Forecasting Model

Chapter 1

An Introduction on Clouds and The Importance of Small-Scale Processes

Clouds are commonplace in the atmosphere, on averaging covering approximately two thirds of the globe (e.g., Stubenrauch et al. 2010). They are commonly observed at all altitudes within the troposphere. Clouds are composed of either liquid droplets, ice particles, or both. The cloud phase is primarily determined by temperature. At temperatures greater than 0°C, clouds are only composed of liquid droplets (liquid phase clouds). In contrast, clouds are only composed of ice particles (ice phase clouds) at temperatures less than -40°C. Airborne aerosols can act as cloud condensation nuclei or ice nuclei (IN), and are required for the initiation of cloud particles. In order for a cloud to form, the air must cool or moisten until supersaturation occurs. Clouds often form within regions of rising air, since rising air will cool as a consequence of adiabatic expansion.

Clouds are often characterized by their microphysical characteristics, such as by particle size and number concentration. Microphysical properties can have major impacts on large scale cloud regimes. Lifetimes of clouds have been shown to increase in regions having high aerosol concentrations, which produce high cloud droplet number concentrations and inhibit precipitation by reducing collision-coalescence (Albrecht 1989). Twomey (1977) showed that increasing the number concentration of cloud droplets can increase the reflectance of clouds, which can have a cooling effect for thin clouds and a warming effect for moderately thick clouds. Such large scale cloud features, resulting from their microphysical properties, can have major implications on weather and climate. Thus, it is crucial to improve our knowledge of cloud microphysical processes in order to improve weather forecasting and global climate predictions. This is further illustrated by the fact that clouds, aerosols, and their interconnectedness are a large source of uncertainty in future climate projections (IPCC 2013).

Two separate models are evaluated, namely, the Weather Research and Forecasting model (WRF) and Community Atmosphere Model version 5 (CAM5). WRF is commonly used for regional weather forecasting, whereas CAM5 is used for global climate prediction. Both models require cloud microphysics parameterizations, which parameterize cloud microphysical processes (which occur on the scale of meters and smaller) at relatively large spatial scales for the sake of computational efficiency. Horizontal spatial scales resolved in simulations are commonly on the order of kilometers to hundreds of kilometers for weather and climate models, respectively, although scaling can vary considerably depending on the application. In contrast, in situ airborne observations utilized in this study have horizontal resolutions on the order of 100 m. An inherent difference in scaling exists between the observations and simulations, which is addressed in each respective section.

The purpose of the following two studies is to examine cloud microphysical properties using in situ airborne observations and compare results with model simulations. Considerable focus is put on observations of relative humidity (RH) and its treatment in simulations. Local RH has major impacts on cloud genesis, lifetime, and thickness, and is a major determinant of clouds' microphysical properties (e.g., Gierens 2003; Koop et al. 2000). Chapter 2 focuses on RH in the upper troposphere during episodes of convective activity and its treatment in WRF. Emphasis is put on the relationship between RH and vertical air motion, which can dramatically perturb temperature due to adiabatic expansion/compression. Chapter 3 focuses on RH over the Southern Ocean at temperatures relevant for clouds containing ice and/or supercooled liquid (<0°C) and its treatment in CAM5. Emphasis is put on the distribution of RH within varying cloud fractions and cloud phases. Persistent low-level cloud regimes have been observed in the region (e.g., Mace et al. 2007), which currently are poorly represented in climate models (Bodas-Salcedo et al. 2014).

Chapter 2

Dynamical Conditions of Ice Supersaturation in Convective Cirrus: Comparing In Situ Observations with WRF Simulations

Adapted from: D'Alessandro J. J., et al. (2017): Dynamical conditions of ice supersaturation and ice nucleation in convective systems: A comparative analysis between in situ aircraft observations and WRF simulations, *J. Geophys. Res. Atmos.*, doi:10.1002/2016JD025994.

2.1 Background: Microphysical Characteristics of Convective Cirrus

Cirrus clouds cover approximately 30% of Earth at any given time (Wylie and Menzel 1999), and the global coverage of cirrus clouds plays a critical role in the global radiative budget (Liou 1986; Chen et al. 2000). The microphysical properties of cirrus clouds play a critical role in their radiative properties. These properties consist of ice particle mass, number concentration, size distributions, particle shape and surface roughness. An important factor that directly affects the initiation of ice crystal formation as well as the microphysical properties is the distribution of relative humidity with respect to ice (RHi).

Ice supersaturation (ISS) occurs when the ambient vapor pressure exceeds the saturation vapor pressure with respect to ice (i.e., ISS = RHi > 100%). The formation of ice clouds requires the ambient conditions to be supersaturated with respect to ice. Unlike warm clouds, which are composed entirely of liquid and develop when a fractional amount of supersaturation with respect to water exists, ice cloud formation will not necessarily take place given the precondition of ISS (e.g., Heymsfield et al. 1998; Gierens et al. 1999; Spichtinger et al. 2003; Peter et al. 2006; Krämer et al. 2009; Diao et al. 2014). A critical relative humidity is often established to predict the onset of homogeneous nucleation, based on the water activity of the solution (Koop et al. 2000). Concerning heterogeneous nucleation, ice nuclei (IN) can effectively nucleate ice particles depending on temperature, RHi, and the physical and chemical properties of the IN (Heymsfield and Miloshevich 1995; Pruppacher and Klett 1996; DeMott et al. 2011). The magnitudes of the ambient RHi can also impact size and number concentrations of ice particles formed via both homogeneous and heterogeneous nucleation.

Anvil cirrus clouds are generally composed entirely of ice and are associated with upper level outflow during episodes of convective activity. Three factors are often involved in the processes affecting the microphysical properties of anvil cirrus: RHi, the occurrence of preexisting ice particles, and vertical velocity (Heymsfield et al. 2005). Vertical velocity is important to consider due to rising (sinking) air associated with temperature decrease (increase) as a consequence of adiabatic expansion (compression). Therefore, an examination of vertical velocity is necessary to correctly characterize temperature fluctuations and cooling/heating rates. A notable positive relationship between updraft speeds and RHi has been reported for some time (Heymsfield 1977). Previous studies using composite observations at various vertical levels have suggested temperature to be the most important factor in initiating ISS in the upper troposphere, whereas fluctuations of water vapor are of secondary importance (Kärcher and Haag 2004). More recently, analyses utilizing in situ flight observations showed that by further restricting the analysis to quasi-isobaric levels, water vapor spatial heterogeneities are the dominant factor that determines the locations and magnitudes of ISS rather than temperature spatial heterogeneities (Diao et al. 2014).

Recently, a study utilizing a box model analyzed the time evolution of ice microphysical properties in relation to various constant background vertical velocities (Krämer et al. 2016). The study found that modifying the vertical velocities from 0 to 3 m s^{-1} can significantly impact the evolution of RHi, ice water content (IWC), the effective radius (r_e), and number concentration of ice (Nc), with the resulting IWC, r_e, and Nc varying by several orders of magnitude. Other studies have also investigated the competition between various ice nucleation and freezing modes, and their impacts on properties such RHi, IWC, and Nc (Gierens 2003; Eidhammer et al. 2009;

Barahona and Nenes 2009). Gierens (2003) used a box model and showed that whether heterogeneous or homogeneous freezing dominates is determined by temperature, updraft speed, ambient pressure, and ISS. The author noted that vertical velocity could differentiate whether heterogeneous or homogeneous nucleation would occur, with stronger updrafts (on the order of 0.1 m s^{-1} for pristine conditions to 1 m s^{-1} for polluted conditions) generally associated with homogeneous nucleation. The significance of vertical velocity as a diagnostic parameter for ice microphysical properties, however, is still uncertain. Muhlbauer et al. (2014) analyzed in situ observations of ice microphysical properties of cirrus clouds formed during various synoptic conditions and found that the probability density functions (PDFs) of vertical velocity perturbations were similar among cirrus associated with strong convection (anvil cirrus), frontal lifting around midlatitude cyclones, and upper level ridges, while particle size distributions were found to have distinct differences associated with these mesoscale or synoptic conditions. Because of this, Muhlbauer et al. (2014) concluded that vertical velocity is a poor predictive parameter for ice cloud microphysical properties.

The purpose of this study is to evaluate the frequency and magnitude of the simulated ISS in the upper troposphere in the Weather Research and Forecasting (WRF) model and compare results with in situ observations. Previously, Diao et al. (2015) examined in situ airborne observations of RHi in the upper troposphere/lower stratosphere over North America and found the average occurrence frequencies of ISS to be ~1.5–2 times greater on the anticyclonic side of the polar jet stream compared with the cyclonic side. This study aims to similarly examine the occurrence and magnitude of RHi in convective regions. Additionally, the sensitivity of ISS to local cooling rates driven by adiabatic expansion is examined by directly relating ISS to vertical velocity within convective cirrus, anvil cirrus, and surrounding convective systems. Examination of the RHi-vertical velocity relationship at larger spatial scales is certainly warranted; however, the purpose of this study is to examine this relationship at the microscale by comparing in situ observations and WRF simulations. We will mainly compare the correlations among ISS, vertical velocity, and ice microphysical properties (i.e., IWC and Nc). Sensitivity tests to address whether the compared correlations represent general physical processes or show a strong dependence on spatial/temporal sampling are also discussed. Overall, our comparison results help to evaluate the general performance of various microphysics schemes in the WRF model.

2.2 Datasets and Simulations

In situ measurements were taken by the National Science Foundation (NSF)/National Center for Atmospheric Research (NCAR) Gulfstream-V (GV) research aircraft during the NSF Deep Convective Clouds and Chemistry (DC3) campaign. The DC3 campaign took place during 18 May to 30 June 2012 at the following locations: northeastern Colorado, northern Alabama, west Texas, and central Oklahoma. Barth et al. (2015) provides a detailed description of the DC3 campaign.

A total of 22 flights were performed by the GV aircraft, each with 1 s merged data (~250 m horizontal scale for 1 Hz data) from a suite of instrumentation. Water vapor measurements were taken from the 25 Hz, open-path Vertical Cavity Surface Emitting Laser (VCSEL) hygrometer. Water vapor measurements are averaged to 1 Hz for consistency with other measurements. The accuracy and precision of water vapor measurements are ~6% and ≤1%, respectively. Ice water content (IWC) is derived from the Fast Two-Dimensional Optical Array cloud probe (2DC), which uses high-speed electronics and a 64-element 25 μm resolution diode array in order to shadow particles at the sampling speeds of the GV. To reduce uncertainties, only the particles that shadow a minimum of three or more diodes (having a diameter of 62.5 μm or more) are included in the data set. The effects of shattered ice particles on the exterior arms or inlet shields of cloud probes are potentially important when analyzing airborne ice particle measurements (e.g., Jensen et al. 2009). The 2DC is equipped with antishattering tips to minimize these effects. However, there is no perfect solution to completely eliminate shattering, as previously reported (Korolev et al. 2013). This study focuses on IWC when evaluating ice particle measurements, which should result in lower uncertainties from ice particle shattering than number concentrations. The IWC is derived from diameter and number concentration measured by 2DC following Brown and Francis (1995). Temperature measurements were taken by a Rosemount temperature probe with the accuracy and precision of ~ ±0.3 K and ~0.01 K, respectively. Vertical velocity measurements were derived from a suite of instrumentation, including the Radome Gust Wind Package, pitot tubes, temperature probe, inertial reference unit, and the differential Global Positioning System, which has a precision of ~0.012 m s^{-1} and accuracy of ~0.15–0.3 m s^{-1}. According to an in-flight intercomparison conducted by the NCAR Research Aviation Facility between the GV vertical velocity measurements and the NCAR Laser Air Motion Sensor instrument, very good agreement is shown between them. RHi is derived from water vapor mixing ratio, pressure, and temperature following the calculations in Murphy and Koop (2005). When combining the uncertainties in water vapor and temperature measurements, the uncertainty of RHi for the sampling range of 233.15 K to 207 K is ~6.9%–7.4%.

2.2.1 WRF simulations

The Advanced Research WRF model simulations (version 3.7) were run with four microphysics schemes, Morrison et al. (2009), a modified Morrison, Thompson et al. (2008), and Thompson and Eidhammer (2014) (hereafter referred to as Morrison, Morrison-125%, Thompson, and Thompson-aerosol, respectively) using the Global Forecast System (GFS) 6-hourly 0.5° × 0.5° initialization data. Each simulation has a parent domain (12 km horizontal grid spacing) and a nested domain (2.4 km horizontal grid spacing) with 40 vertical levels and a pressure top of 30 hPa (except for 70 hPa in Thompson-aerosol). Simulations were run starting on

19 May 2012 at 0000 UTC for 30 h. We also conducted 800 m horizontal grid spacing nested domain simulations for all microphysics schemes, and the sensitivity tests show no significant impacts on our conclusions. The time steps for the parent and two nested domains are 60, 12, and 4 s, respectively (except for Thompson-aerosol with 30, 6, and 2 s, respectively). Figure 1A shows the parent and nested domains, as well as the DC3 flight paths. Model longwave radiation (Mlawer et al. 1997), the NOAH land surface model (Chen and Dudhia 2001), and the Mellor-Yamada-Janjic planetary boundary layer scheme (Janjić 1994). Both Morrison and Thompson include number concentrations of newly formed ice crystals predicted by the Cooper (1986) parameterization, which is solely a prognostic function of temperature, $Nc_i = 0.005 \exp[0.304 * (T_0 — T)]$, where Nc_i is the number of ice crystals initiated (L^{-1}), T_0 is 273.15 K, and T is the ambient temperature in Kelvin. Morrison and Thompson initiate the Cooper parameterization when RHi exceeds 108% and 125% (or when liquid saturation is reached below 265.15 K and 261.15 K), respectively, while Thompson-aerosol does not include the Cooper parameterization. The only modification in Morrison-125% is to increase the RHi threshold for initiating the Cooper parameterization from the default value (RHi of 108%) to RHi of 125%. Additional restrictions on the Cooper parameterization are applied. For example, Morrison and Thompson restrict the number concentration of ice particles formed via the Cooper parameterization to 500 L^{-1} and 250 L^{-1}, respectively, and the mass-weighted mean size of cloud ice may not exceed 300 μm in Thompson. Both Morrison and Thompson allow for homogeneous and heterogeneous freezing of cloud droplets and rain, where heterogeneous freezing is parameterized following Bigg (1953) (for both schemes) and homogeneous freezing occurs instantaneously at -40°C and -38°C, respectively. Frozen cloud droplets and rain can potentially account for a significant portion of the total Nc in and around convection systems, where liquid droplets can be lofted to the homogeneous freezing level.

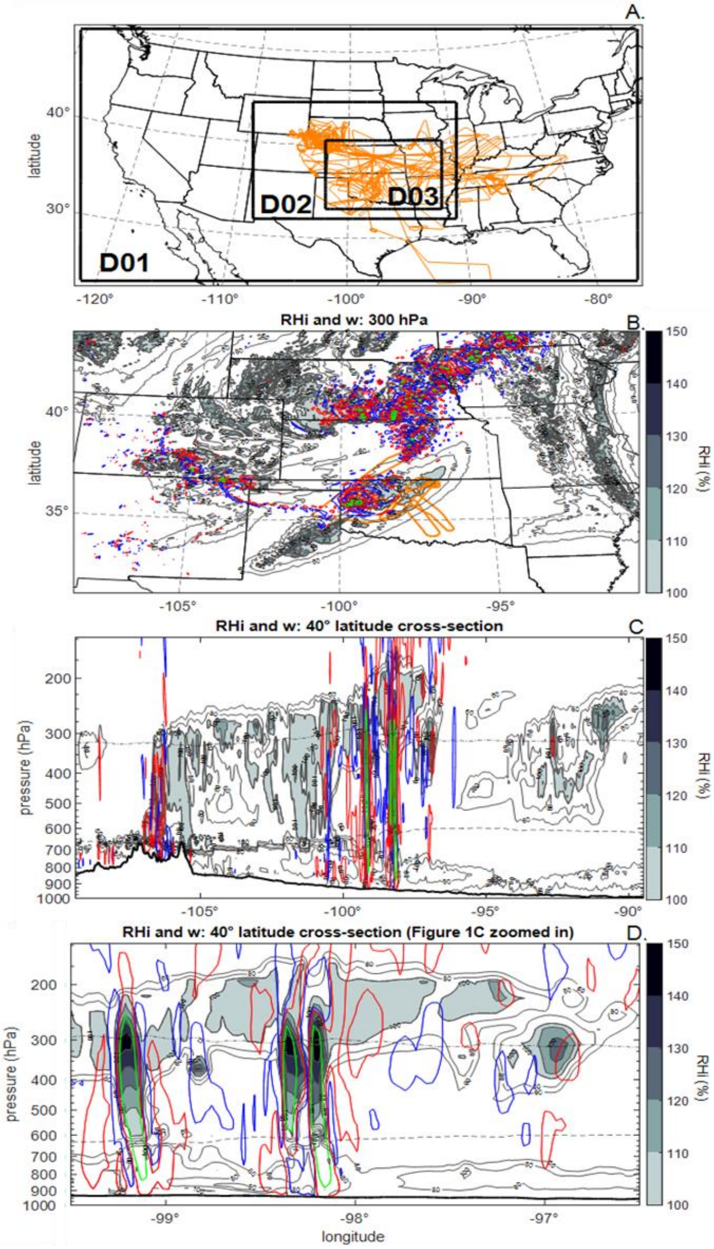

Figure 1. The parent and nested domains for WRF simulations with all flight tracks from DC3 (thin orange lines) (A). Distributions of RHi and vertical velocity in a horizontal cross section at 300 hPa (B) and in a vertical cross section at 40°N latitude (C and D), based on Thompson with the 2.4 km nested domain on 20 May 2012 at 0000 UTC. The 19 May flight track (thick orange line) is shown in Figure 1B. The gray contours show RHi gradient, with shaded gray colors representing ice supersaturated regions. Vertical velocity contours are shown for -0.5 m s^{-1} (blue), +0.5 m s^{-1} (red), and ±5 m s^{-1} (green). The dashed and dash-dotted lines are the 0°C and -40°C isotherms, respectively.

The treatment of deposition/sublimation rates for ice and snow in Morrison is similar to Harrington et al. (1995), Ferrier (1994), and Reisner et al. (1998), whereas the calculations in Thompson are based on Srivastava and Coen (1992).

Thompson-aerosol is similar to Thompson but explicitly treats aerosols categorized as either "water friendly" (hygroscopic) or "ice friendly" (nonhygroscopic), allowing for the activation of aerosols as both IN and cloud condensation nuclei, initialized with the climatological aerosol data set. As described in Thompson and Eidhammer (2014), deposition freezing (below water saturation) is parameterized with Phillips et al. (2008), while immersion freezing (at or above water saturation) is now parameterized with DeMott et al. (2011). Homogeneous nucleation of the water friendly aerosols is parameterized with Koop et al. (2000). At the temperatures considered in this study (≤ -40°C), the DeMott parameterization will not activate since homogeneous nucleation initiates at lower RHi compared with the DeMott parameterization. Thus, while the Cooper parameterization in the other three microphysics schemes implicitly includes heterogeneous and homogeneous nucleation, Thompson-aerosol allows for explicit simulations of the competition between heterogeneous and homogenous nucleation.

All four microphysics schemes allow for supersaturation with respect to ice, without applying the saturation adjustment to the ice hydrometeors. In addition, all microphysics schemes calculate the saturation vapor pressure with respect to ice following Flatau et al. (1992). Differences in the calculated RHi between Murphy and Koop (2005) and Flatau et al. (1992) are minimal, ranging from ~0% to 0.34% at the combined water vapor and temperature ranges sampled by the DC3 observations between -40°C and -65.8°C. However, there are somewhat larger differences in liquid saturation between Flatau et al. (1992) and Murphy and Koop (2005). Slightly higher RHi values of 1.17%–15.75% and 1.14%–6.42% occur at liquid saturation in Thompson and Morrison based on Flatau et al. (1992) compared with Murphy and Koop (2005), respectively. This explains the occurrence of a small number of points in the simulations with RHi exceeding the liquid saturation line calculated by Murphy and Koop (2005).

Our main analyses are based on simulations over the Great Plains region on 19 May 2012, during a convective episode throughout the area. The event was marked by several high wind (>33 m s^{-1}) and hail (diameter > 5 cm) reports stretching from Southern Oklahoma to Western Iowa. The GV took observations on this day over Oklahoma, where a squall line associated with the high winds and large hail occurred. The event was marked by elevated instability and widespread values of convective available potential energy above 1000 J kg^{-1} throughout most of the region. A composite data set for each simulation is obtained by combining outputs at four times, 1800, 2100, 0000, and 0300 UTC from 19 to 20 May 2012 (i.e., 1–10 P.M. local time on 19 May 2012). These outputs are chosen from the simulations to obtain data sampled over 9 h of a convective episode, which included multiple clusters of thunderstorms and a well-developed squall line in the southern domain (see Figure 1B). High water vapor concentrations from the WRF simulations were found to have similar spatial distributions to those seen in the GOES 13 satellite imagery. Sensitivity tests of another set of realistic case simulations (11–12 June 2012) are also examined, which show consistent conclusions for the statistical distributions of ISS and its correlation with vertical velocity.

To visualize the RHi and vertical velocity (w) fields from the simulations, Figures 1B and 1C show RHi and w spatial distributions for the entire nested domain using Thompson. At 300 hPa, gravity waves are seen surrounding the strongest updrafts and downdrafts, and ISS is often collocated with relatively high fluctuations in w (e.g., between 100°W and 95°W) (Figure 1B). The vertical cross-section view at 40°N (Figures 1C and 1D) reveals a deep convective structure with w of ±5 m s^{-1} extending from 875 hPa to 250 hPa. The higher RHi (e.g., >140%) appears to occur almost exclusively at the upper tropospheric levels within regions of strong updrafts, while weaker updrafts (e.g., w > 0.5 m s^{-1} at 97°W near 300 hPa) also collocate with RHi > 130%.

2.2.2 Composite datasets for the comparisons between observations and simulations

To conduct the comparison, similar restrictions are imposed on the composite data sets for in situ observations (1 Hz data from 22 flights) and WRF simulations (all grid points in the nested domain for four time outputs). Data analyses are restricted to regions where the temperature is less than or equal to -40°C to prevent the sampling of mixed-phase clouds (MPC) for the purposes of solely analyzing the distributions of RHi and microphysical properties of ice particles. The minimum IWC reported for one particle per 1 Hz measurements from the 2DC probe in the DC3 campaign is used to define in-cloud conditions in both observations and simulations (i.e., IWC $\geq 3.82 \times 10^{-5}$ g m^{-3}), whereas clear-sky conditions are defined when IWC is less than this threshold. The four microphysics schemes considered in this study predict mass mixing ratios for three types of frozen hydrometeors: ice, snow, and graupel. For the simulations, IWC is treated as the sum of these quantities. Similarly, Nc is treated as the total number of the frozen hydrometeors. Morrison and Morrison-125% predict Nc for ice, snow, and graupel, whereas Thompson and Thompson-aerosol only predict Nc for ice. The observational data are restricted to below the tropopause, where the tropopause height is based on the National Centers for Environmental Prediction GFS-FNL (final) data set interpolated onto the GV aircraft position and time. Simulation data sets are restricted to regions where ambient pressure is ≥148 hPa (i.e., the lowest pressure sampled by GV in DC3). With these restrictions imposed, the total number of 1 Hz observations in 22 flights amounts to ~67 h, compared with ~106 grid points in the 2.4 km nested domain for four time outputs. We also examined the correlations between ISS probabilities and w by using the in situ observations on board the NASA DC8 research aircraft during the DC3 campaign and found consistent correlations between ISS frequencies and w as those shown in the composite data set from the GV aircraft.

2.3 Results

2.3.1 RHi distributions at clear-sky and in-cloud conditions

Occurrences of RHi are shown for both in-cloud and clear-sky conditions (Figure 2, first and second columns).

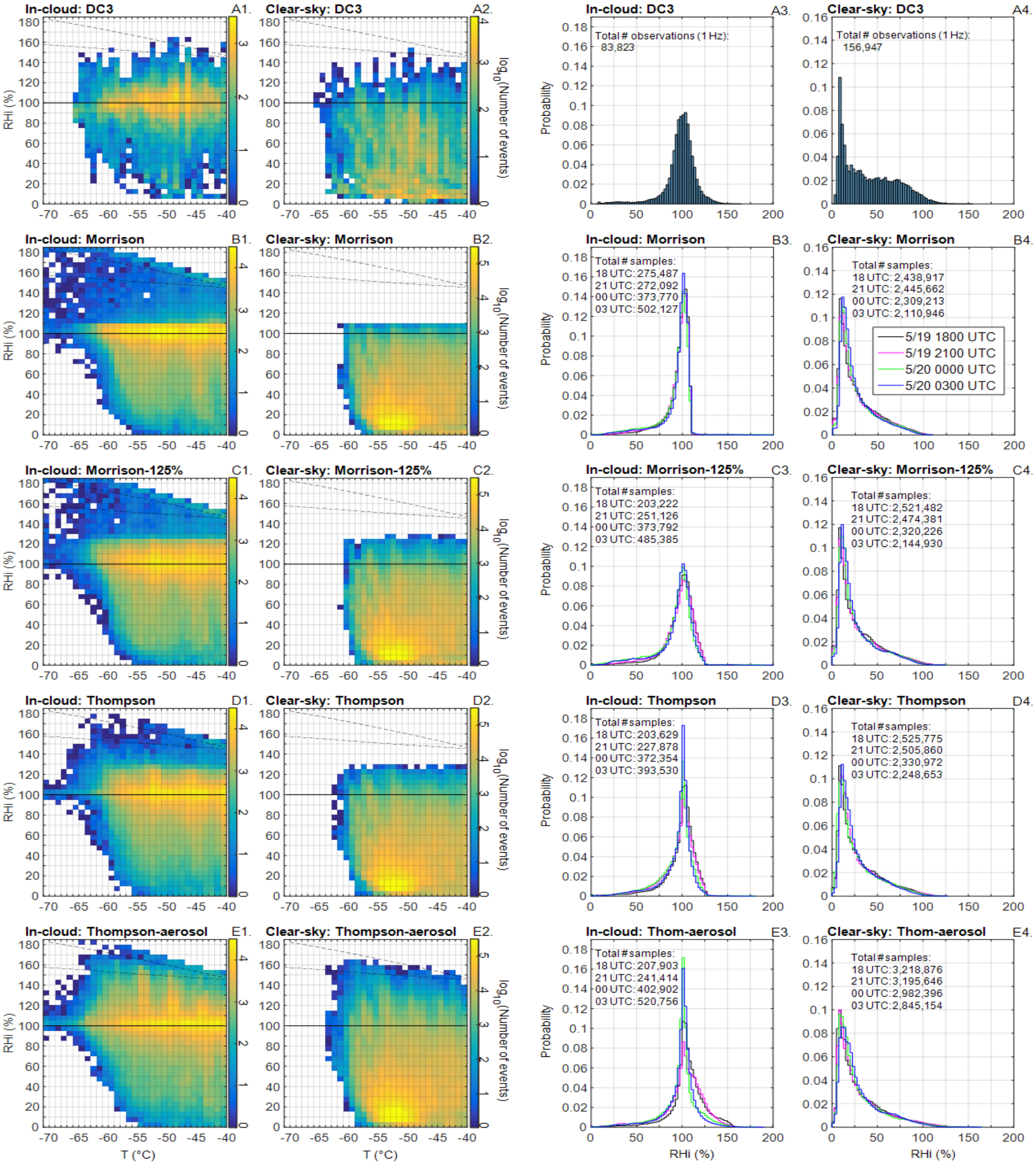

Figure 2. Occurrences of RHi with respect to temperature and probability density functions (PDFs) of RHi for DC3, Morrison, Morrison-125%, Thompson, and Thompson-aerosol. The comparisons for in-cloud and clear-sky conditions are shown separately. The RHi-T distributions (first and second columns) are based on the composite of four time outputs from WRF simulations, with RHi and T binned by 5% and 1 K, respectively. The PDFs of RHi (third and fourth columns) show these four WRF time outputs individually in different colored lines, with RHi binned by 2.5%. In the RHi-T distributions, the solid and dashed lines represent the saturations with respect to ice and with respect to liquid water, respectively. The homogeneous freezing line (dash-dotted) is based on Koop et al. (2000) with deliquesced particles at the diameters of 0.5 μm.

Throughout the entire temperature distribution shown for the observations, RHi ranges from ~10%–160% and ~5%–150% for in-cloud and clear-sky conditions, respectively. The few occurrences of RHi above the liquid saturation line are within the range of measurement uncertainties. Similar to the observations, the simulated in-cloud RHi most frequently occur within ±5% to ±15% of ice saturation, yet they all extend to higher values (RHi around 180%) compared with the observations. Additionally, all of the simulations show a slight increase in RHi occurrences around the liquid saturation line, which may be attributed to regions near and within the convective core of deep convective systems (as illustrated in Figures 1B–1D), where aircraft would avoid sampling due to strong turbulence. When analyzing simulations of an idealized squall line scenario without synoptic-scale dynamic forcing and radiative forcing, we found that the simulations did not capture ISS at clear-sky conditions. Thus, the capability of capturing ISS at both clear-sky and in-cloud conditions in the WRF simulations suggests that larger-scale dynamical forcings and/or radiative forcings play an important role in ISS formation.

The unrealistic limits of the clear-sky RHi magnitudes in Morrison, Morrison-125%, and Thompson are also the respective RHi thresholds for initiating the Cooper parameterization (i.e., RHi of 108%, 125%, and 125%, respectively). Similarly, sharp gradients are seen for in-cloud RHi distributions. In comparison, Thompson-aerosol without the Cooper parameterization shows clear-sky ISS extending to the liquid saturation line, with ISS as high as ~60% occurring at colder temperatures. By increasing the default threshold of initiating the Cooper parameterization, Morrison-125% produces more comparable results to the observations than the default Morrison in terms of the magnitude and frequency of ISS allowed at the relatively higher RHi (>108%).

The PDFs of RHi are compared among observations and four individual WRF time outputs (Figure 2, third and fourth columns). For in-cloud conditions, the PDF of RHi for DC3 data set centers at ~100%, which is consistent with previous in situ observations of in-cloud RHi distributions (Ovarlez et al. 2002a; Krämer et al. 2009; Diao et al. 2014). Morrison, Thompson, and Thompson-aerosol all have much higher in-cloud RHi probabilities (~0.16–0.18) centered at ice saturation compared with that of observations (~0.09), while Morrison-125% has the most comparable RHi frequency (~0.1) at ice saturation. The variations in RHi distributions with respect to different time outputs appear minimal for the simulations, where the most notable change is the narrower peaks of PDF centered at RHi = 100% along the time evolution. Thompson-aerosol is the only scheme that allows for noticeable RHi probabilities at RHi > 125% as seen in the observations, especially for the earlier time outputs, even though this scheme shows slightly higher probabilities (e.g., ~0.01–0.02 at RHi = 130%) at this RHi range than those in the observations (~0.01 at RHi = 130%).

For clear-sky conditions, PDFs of RHi for the simulations and observations both peak around 10%. However, the decay of RHi frequency from RHi of 20% to 80% is much sharper in all the simulations, while the RHi frequency appears almost constant from 40% to 80% in the observations. In addition, observations show higher probabilities of clear-sky ISS than simulations, with Thompson-aerosol having the highest clear-sky ISS frequency among the simulations. These discrepancies between observations and simulations may be subject to sampling differences between DC3 and WRF, since the GV aircraft often sampled regions within 24 h of convective activity, whereas the entire nested domain of the WRF simulations is included in the data sets (as shown in Figure 1). However, we note that the lack of clear-sky ISS occurrence frequencies in the simulations is not due to a lack of clear-sky sampling. In fact, the total numbers of samples (i.e., 1 Hz data and grid points) for in-cloud and clear-sky conditions are proportionally about 1:2 in DC3 and about 1:7 in the WRF simulations.

2.3.2. Temperature, vertical velocity, IWC and Nc distributions inside ISS conditions

The normalized frequency distributions of temperature, w, IWC, and Nc are shown for various ranges of ISS (Figures 3A–3D and 3E–3H). Temperature distributions of the four simulations are similarly well dispersed, whereas observations sampled more frequently at -50°C to -46°C than at -46°C to -40°C.

The PDFs of w for in-cloud (clear-sky) ISS conditions (Figures 3C and 3D) are centered at 0.34 m s^{-1} (-0.02 m s^{-1}) and ~0.14 m s^{-1} (~0.01 m s^{-1}) for observations and simulations, respectively, showing a slightly higher average w for in-cloud ISS in the observations. The cumulative frequency distributions (CFDs) of w for in-cloud ISS show strong sensitivities to ISS magnitudes in Morrison and Morrison-125%, with their 90th percentile of w increasing from 0.25 m s^{-1} to 1–2 m s^{-1} when ISS increases from below to above 20% (Figure 3E). For clear-sky conditions, the CFDs of w are similar for different ISS ranges (>20% and ≤20%) in the observations and simulations (Figure 3F). This suggests that vertical velocity, as a parameter, may be a poor predictor for the magnitude of clear-sky ISS. Standard deviations of ~0.9 m s^{-1} are seen for all the simulations compared to ~0.57 m s^{-1} in the observations as a result of the intense updrafts and downdrafts sampled in simulations (up to ~50 m s^{-1} in Morrison and Morrison-125%, ~40 m s^{-1} in Thompson and Thompson-aerosol, and as low as ~ -17 m s^{-1} in all the simulations).

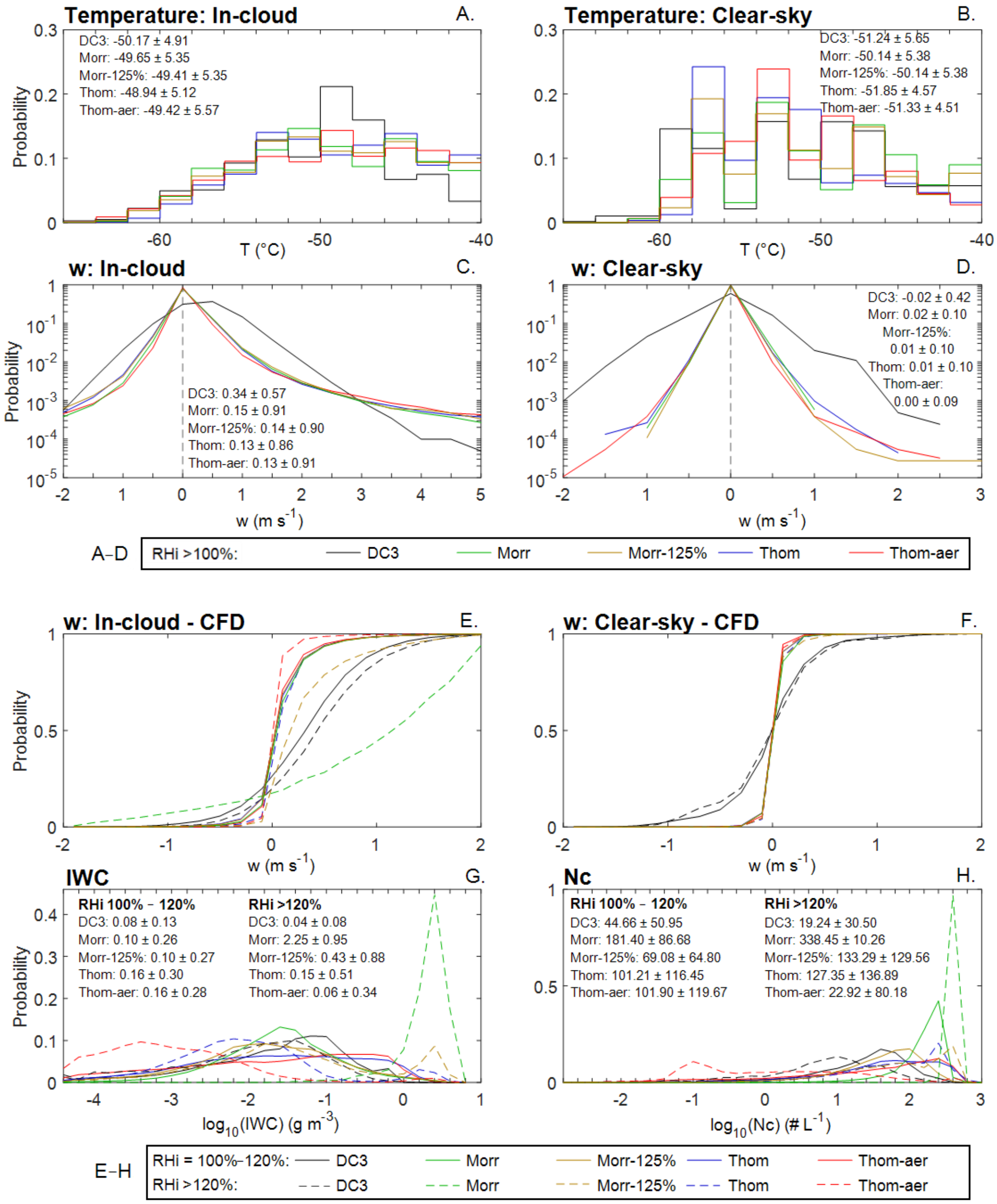

Figure 3. Probability distributions of temperature, w, IWC, and Nc for various ranges of ISS at in-cloud and clear-sky conditions. Normalized frequency distributions of temperature, IWC, Nc, and w are binned by 2°C, 0.2 g m^{-3}, 0.2 L^{-1}, and 0.5 m s^{-1}, respectively. The CFDs of w are restricted to ±2 m s^{-1} and are binned by 0.2 m s^{-1}. In Figures 3A–D, the solid color lines represent RHi > 100% for various data sets. In Figures 3E–H, the solid and dashed lines represent RHi = 100%–120% and RHi > 120%, respectively. The mean and standard deviation (±σ) of each variable are provided in their respective figures. We note that the means and standard deviations for in-cloud and clear-sky w are calculated over the entire distribution of their respective data sets.

Large differences in IWC and Nc distributions exist among the observations and simulations for different ranges of ISS. In Morrison, the IWC distribution peaks at ~0.025 g m^{-3} for ISS ≤ 20%, and this peak shifts to a significantly larger value at ~2.5 g m^{-3} for ISS > 20%, which is ~1.5 orders of magnitude greater than that in the observations (Figure 3G). Thompson-aerosol has the opposite trend compared with Morrison, as it shows a decreasing IWC trend with increasing ISS magnitudes. In addition, the average Nc in Thompson-aerosol decreases by more than a factor of 4 from ISS ≤ 20% to ISS > 20%. In fact, Thompson-aerosol is the only scheme that shows both decreasing IWC and Nc with increasing ISS, similar to the observations.

Consequences of the different IWC and Nc distributions among the various simulations can be seen in the CFDs of w for in-cloud ISS conditions. When higher IWC and/or Nc exist, higher w are often seen to be associated with in-cloud ISS conditions. For in-cloud ISS > 20%, Morrison and Thompson-aerosol have ~20% and 80% of w below 0.25 m s^{-1}, respectively, likely due to the higher IWC and Nc values in Morrison. These results are consistent with the previous theoretical calculations, which showed that ice cloud properties can significantly impact the in-cloud ISS distributions due to the depositional growth of ice crystals (Kärcher 2012). Thus, it is crucial to account for in-cloud properties (e.g., IWC and Nc) when evaluating the impacts of various magnitudes of vertical velocity on the characteristics of ISS.

2.3.3 Average vertical velocities for in-cloud ISS conditions

An analysis of average w for in-cloud conditions associated with various magnitudes of ISS is shown in Figure 4. The factors of IWC and Nc are separately accounted for (on the y axis of Figure 4) in order to appropriately evaluate the impacts of various magnitudes of w on ISS. The average w is calculated within each bin of log-scale IWC (or Nc) for various ranges of ISS.

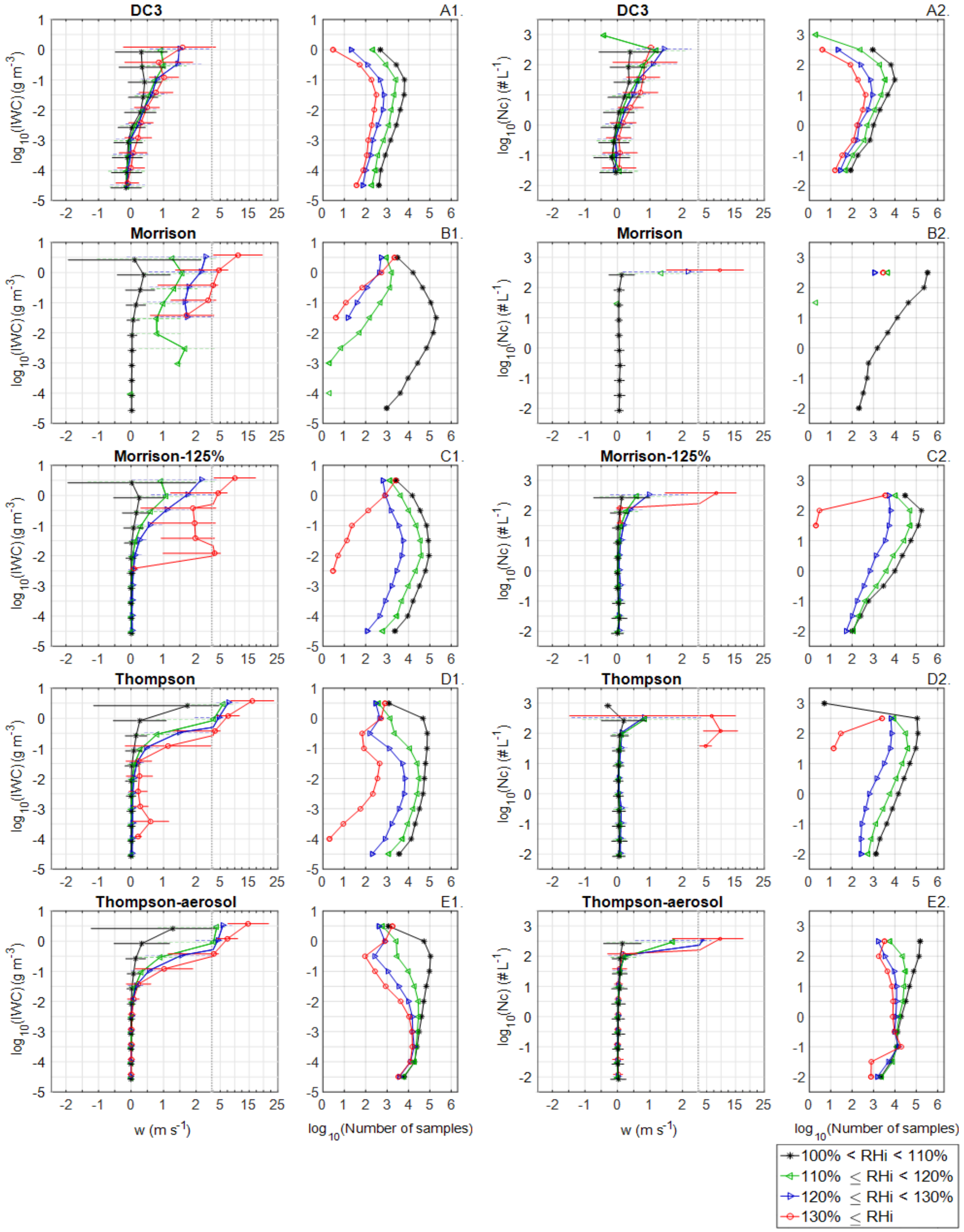

Figure 4. Average vertical velocity (w) binned by (first and second columns) IWC and (third and fourth columns) Nc for different ranges of ISS. Four ranges of ISS are shown in different colored lines. We note that in order to show the different color lines clearly, we slightly shifted them vertically from each other, even though they are binned into the same ranges of IWC and Nc. The horizontal lines represent ±1σ of the w in each bin, and the gray dashed lines highlight various ranges of w. The total number of samples is shown in the second and fourth columns.

We note that since the simulations include frozen hydrometeors at all sizes, the Nc in observations would have a low bias due to the lack of small particles, while the IWC comparisons dominated by larger particles would be less affected.

For observations, the average w increases with the increasing IWC and Nc when they exceed 0.001 g m^{-3} and 1 L^{-1}, respectively. Such increases in the average w with IWC or Nc become even greater as the magnitudes of ISS increase. For simulations, at IWC > 0.01 g m^{-3} or Nc > 100 L^{-1}, the differences in the average w for the various magnitudes of ISS are much larger (i.e., by ~1–15 m s^{-1}) than those in the observations (by ~0.2– 1m s^{-1}). Thus, both observations and simulations show that on average the presence of higher updrafts is required to initiate/maintain the higher magnitudes of in-cloud ISS when associated with relatively high IWC (or Nc), yet the average w in simulations is even higher at the same magnitudes of in-cloud ISS. Note that the Morrison simulation does not have IWC < 10^{-3} g m^{-3} or Nc < 300 L^{-1} at RHi ≥ 108%, due to the initiation of ice crystal formation from the Cooper parameterization. Thompson-aerosol, having the only microphysics scheme without the Cooper parameterization, is the only simulation that captures the low values of IWC (i.e., ~3×10^{-5} g m^{-3}) and Nc (~0.01 L^{-1}) for each interval of ISS shown.

2.3.4 Correlations between the probabilities of ISS and w for in-cloud conditions

To examine the physical processes controlling ISS formation in the WRF simulations, we compare the simulated correlations between ISS probabilities and w with those from observations for in-cloud conditions (Figures 5 and 6). The comparisons between observations and simulations in Figures 5 and 6 are restricted to the same ranges of w, which exclude the extreme updrafts and downdrafts sampled in the simulations but not in the observations as discussed prior (Figure 3). By restricting the analysis to the same ranges of w, we avoid sampling biases in w for the comparisons. Probabilities of ISS are calculated for each given range of w; that is, the number of occurrences of ISS (within a given 10% interval) are normalized by the total number of occurrences at all RHi ranges for the given range of w. We also control the factors of IWC and Nc because of their potential influences on ISS characteristics. That is, the ISS probabilities are calculated for various scales of w within individual bins of IWC (Figure 5) and Nc (Figure 6).

For the correlations between ISS probabilities and w, observations show that the probabilities of ISS < 10% are relatively similar for various ranges of w given the same ranges of IWC or Nc (except for a few larger IWC and Nc values). In contrast, all the simulations show decreasing probabilities of ISS < 10% correlated with increasing w. For the higher ISS ≥ 10%, observations show higher ISS probabilities in the stronger updrafts than weaker updrafts or downdrafts. The increases in ISS probabilities from weaker to stronger updrafts are even more evident as IWC (or Nc) increases, indicating that stronger updrafts are generally required to generate/maintain ISS when associated with higher IWC or Nc.

Compared with a consistent positive correlation between probabilities of ISS ≥ 10% and w as shown in the observations, simulations show different correlations between IWC > 0.01 g m^{-3} and IWC ≤ 0.01 g m^{-3} (Figure 5). Note that Morrison does not have the lower IWC (108% due to the excess ice crystal formation from the Cooper parameterization. At IWC > 0.01 g m^{-3}, the main difference between the observations and the other three simulations (Morrison-125%, Thompson, and Thompson-aerosol) is that the simulations show much higher probabilities of ISS associated with relatively strong updrafts than those with weak updrafts or downdrafts. In fact, the differences in the probabilities of ISS ≥ 10% increase by 1–1.5 orders of magnitude from downdrafts and weaker updrafts to stronger updrafts in the observations, while those in the simulations increase by 2–4 orders of magnitude. Sensitivity tests on individual flights show consistent results where observations have smaller differences in the probabilities of ISS between lower and higher w than the simulations.

Among the four simulations, Morrison-125% has minimal differences in ISS probabilities between higher and lower w below the RHi threshold of initiating the Cooper parameterization. Such improvement in Morrison-125% cannot be accounted for by only adjusting the Nc upper limit in the scheme (the maximum-allowed concentration of ice). This is seen in Figure 5, row 3, with an additional simulation that changes this limit in the Morrison scheme ($Nc < 500\ L^{-1}$) to the value used in Thompson ($Nc < 250\ L^{-1}$), while using the default RHi threshold of 108% (named as Morrison-Nc250). At $IWC \leq 0.01\ g\ m^{-3}$, simulations show that probabilities of $ISS \geq 10\%$ are surprisingly lower at relatively higher w ($w > 0.5\ m\ s^{-1}$) than those at the lower w, by ~0.5–1 orders of magnitude. These results indicate that compared with observations, simulations have a greater dependence on stronger updrafts for generating and/or maintaining $ISS \geq 10\%$ at the higher IWC values, while an opposite correlation between ISS probabilities and w are shown in the simulations at the lower IWC values. A simulation with twice the number of vertical levels (i.e., 80 levels) was conducted for the Thompson-aerosol scheme (named as Thom-aer-80lev), showing that the differences in the probabilities of $ISS \geq 10\%$ between lower and higher w are still ~2–4 orders of magnitude. In addition, a slight increase in the probabilities of ISS in downdrafts and weaker updrafts by ~0.5 order of magnitude is seen at relatively higher IWC and Nc, suggesting that increasing the number of vertical levels allows for more ISS at lower w for in-cloud conditions.

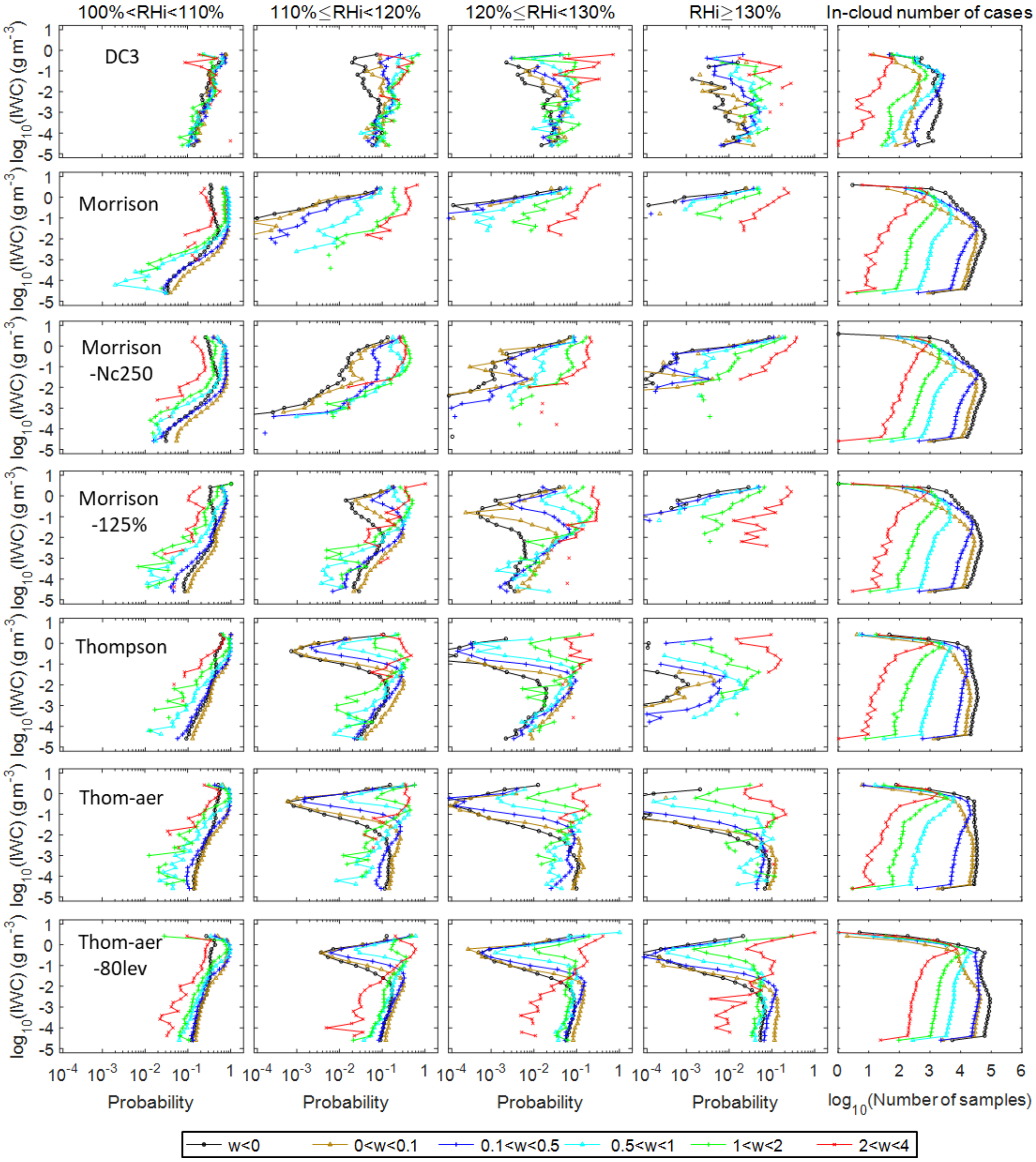

Figure 5. Probabilities of different magnitudes of ISS occurring at various ranges of w (m s^{-1}; shown in different colored lines), controlling for IWC on the y axis. The probability of a given range of ISS occurring is determined by normalizing the number of ISS occurrences in a certain ISS interval at a given range of w and IWC with the total number of occurrences of all RHi at that same range of w and IWC. Probabilities of ISS are shown in the logarithmic scale.

Compared with the analysis controlled by IWC on the ordinate (Figure 5), the analysis controlled by Nc (Figure 6) shows smaller differences in ISS probabilities by 1–2 orders of magnitude between the higher and lower w in all of the simulations, which are comparable to the scales shown in the observations.

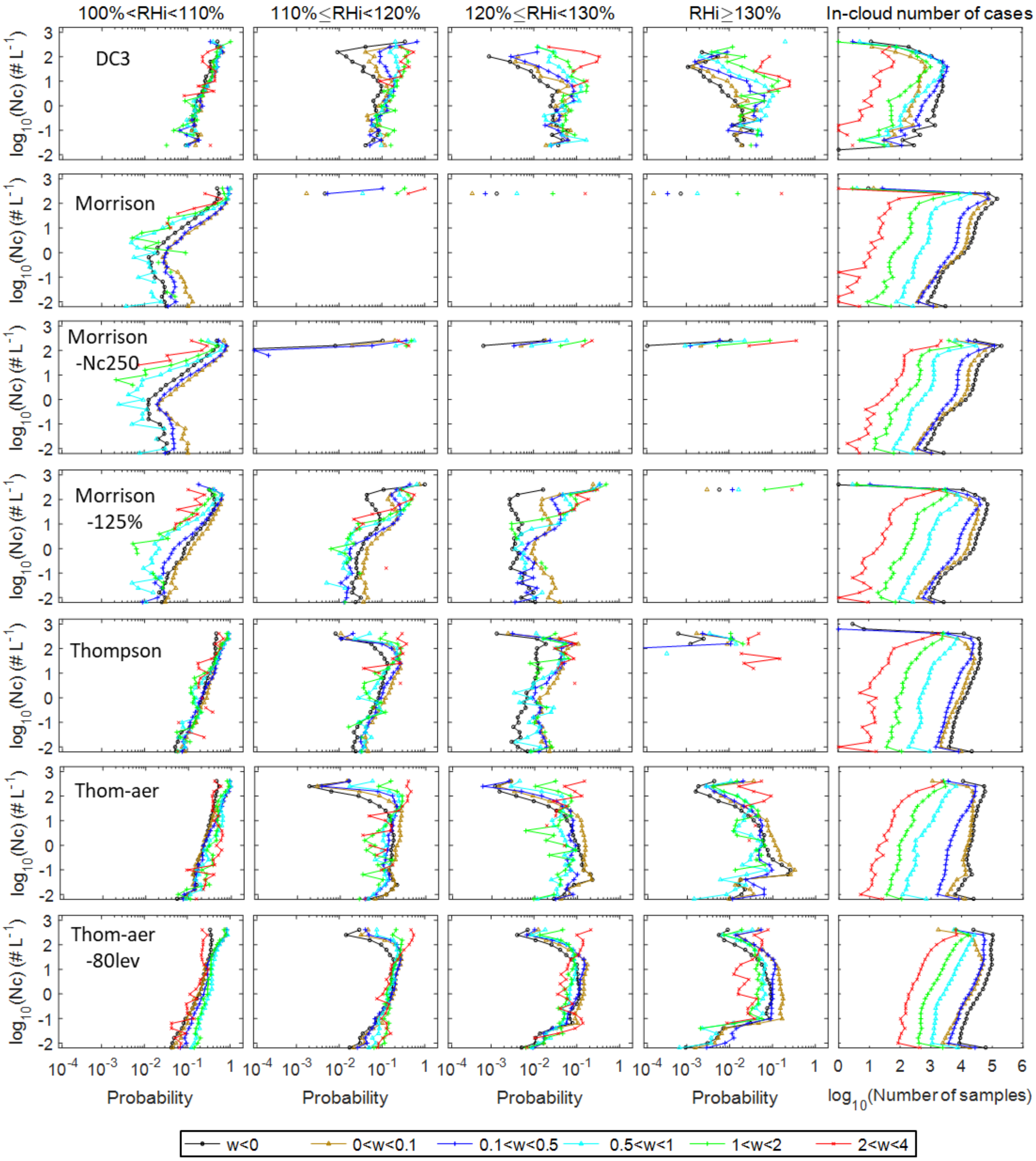

Figure 6. Probabilities of different magnitudes of ISS occurring at various ranges of w (m s^{-1}; shown in different colored lines), controlling for Nc on the y axis. Similar to Figure 5 but controlling for Nc when analyzing the probabilities of different magnitudes of ISS occurring at various ranges of w.

Morrison-125% has increasing probabilities of ISS with increasing Nc for almost all ranges of w, while Thompson, Thompson-aerosol, and Thom-aer-80lev show decreasing ISS probabilities at higher Nc. Thom-aer-80lev has the most comparable results to the observed range of ISS probabilities among all of the simulations when controlling for Nc.

Higher-resolution WRF simulations using the 800 m nested domain are further examined to evaluate the sensitivities of the simulated correlations between ISS probabilities and w to horizontal grid spacings (Figures 7 and 8). The overall correlations between ISS and w are consistent between the 2.4 km and 800 m horizontal grid spacing simulations; that is, the positive and negative correlations between ISS probabilities and w are consistently shown at IWC > 0.01 g m^{-3} and IWC ≤ 0.01 g m^{-3}, respectively. The differences between the two resolutions are mainly shown in the differences of ISS probabilities between higher and lower w. Compared with the 2.4 km simulations, the differences of the probabilities of ISS ≥ 10% in the 800 m simulations decrease (i.e., closer to observations) at higher IWC (>0.01 g m^{-3}) or Nc (>10 L^{-1}) but increase (i.e., more dissimilar to observations) at the lower IWC and Nc.

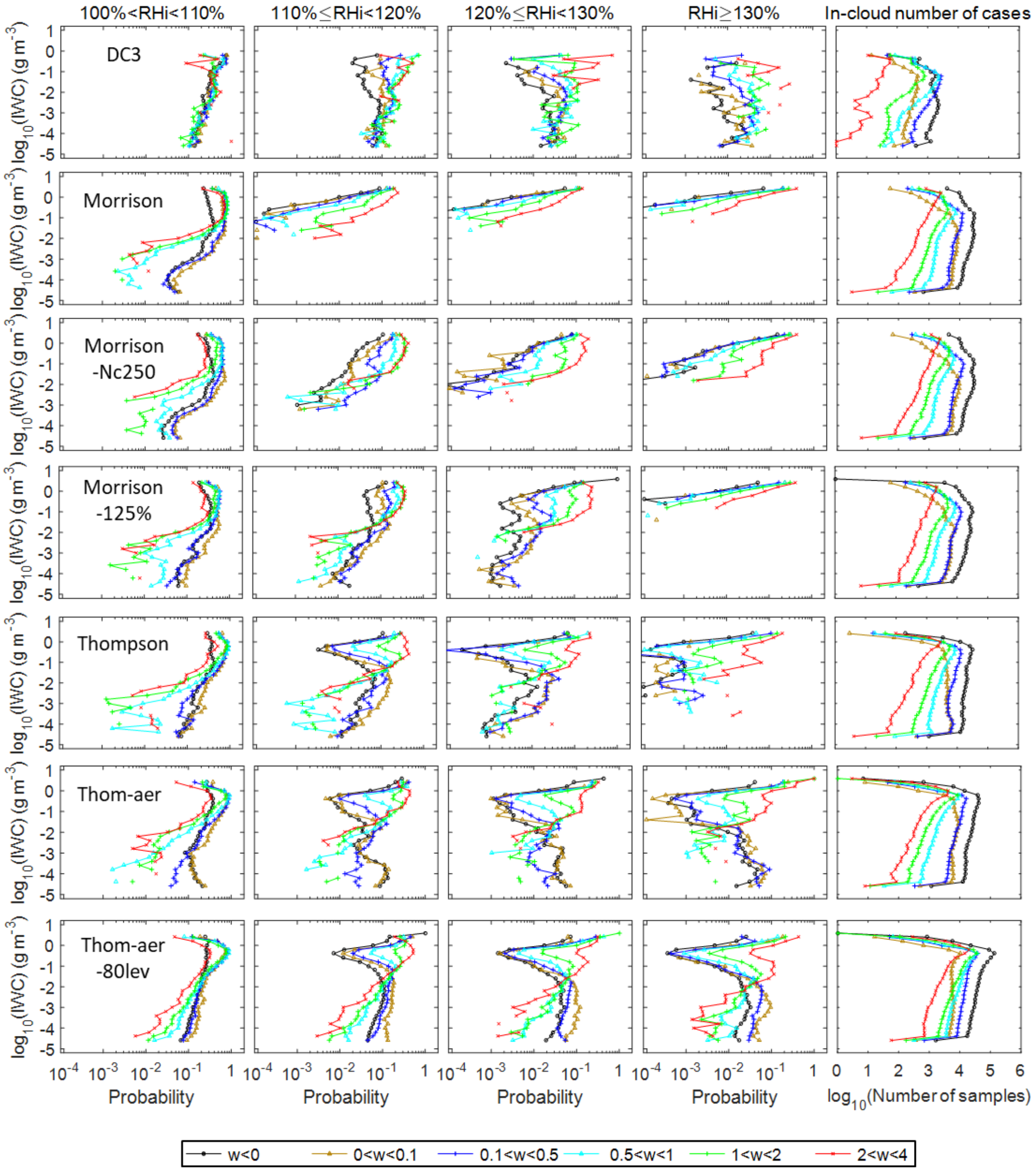

Figure 7. Same as Figure 5 except for using gridded data in a nested domain from higher-resolution WRF simulations, i.e., at 800 m horizontal grid spacing. In this figure, the WRF data sets consist of gridded data from one time output: 20 May 2012 at 0000 UTC.

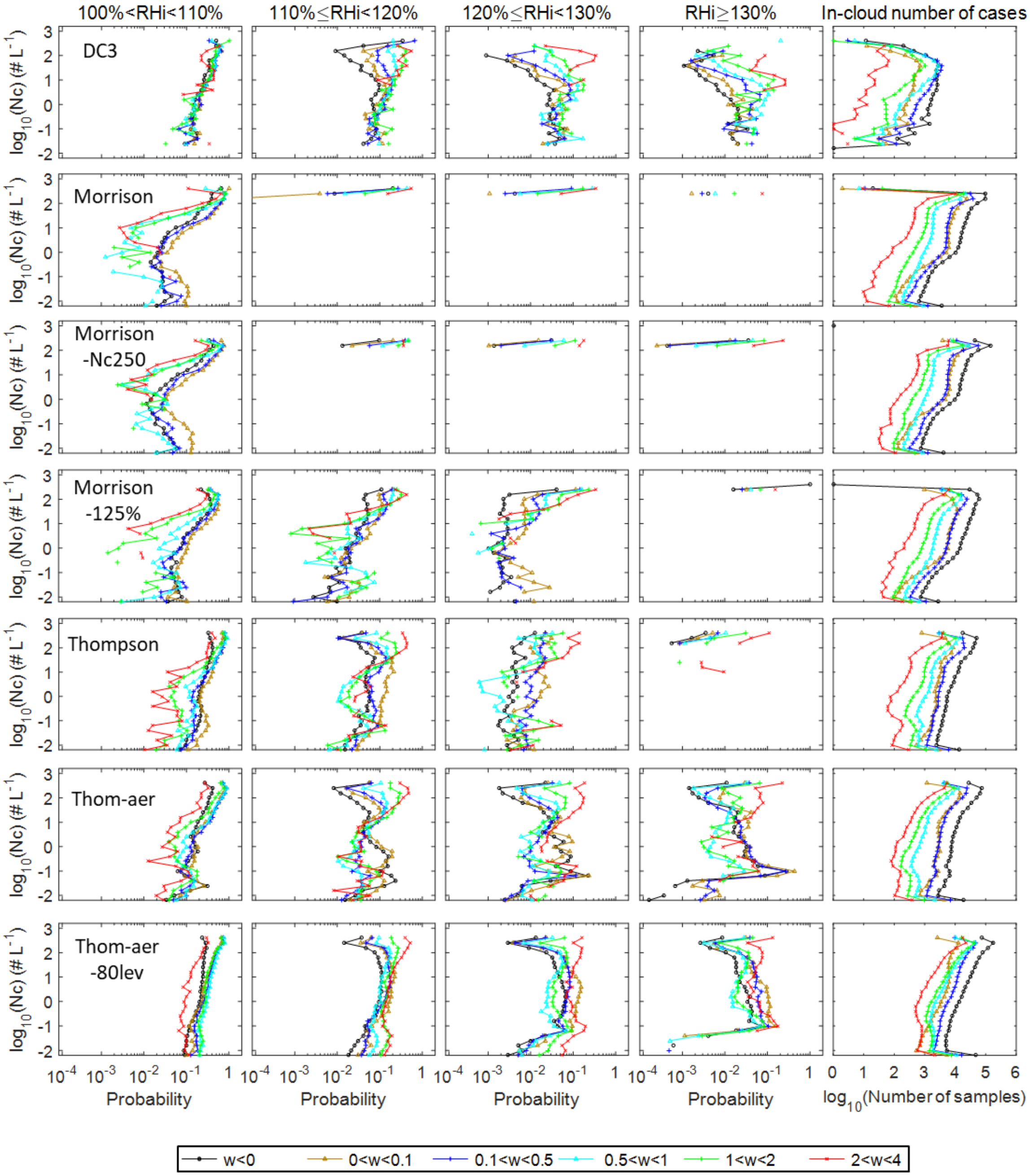

Figure 8. Same as Figure 6 except for using WRF simulations with 800 m horizontal grid spacing. In this figure, the WRF data sets consist of gridded data from one time output: 20 May 2012 at 0000 UTC.

These results suggest that increasing the model resolution does not necessarily produce more comparable results to the observations for all IWC and Nc ranges.

2.3.5 The normalized occurrence frequency of ISS for full range of w

When comparing w at the same magnitudes sampled in observations and simulations in Figures 5–8, the full range of w sampled in WRF simulations is not shown. To provide a depiction of the full range of w for in-cloud conditions, the normalized occurrence frequencies of ISS are further analyzed in relation to all w values, with the factors of IWC and Nc controlled in Figures 9 and 10, respectively. The normalized ISS frequencies are calculated by normalizing the number of ISS data in each IWC-w bin (or Nc-w bin) with the total number of RHi data in that bin, and results are shown in four ranges of ISS from 0–10%, 10%–20%, 20%–30% to ≥30%.

In Figure 9, both observations and WRF simulations show increasing occurrence frequencies of ISS at higher updraft speeds and larger IWC, and the higher ISS frequencies in stronger updrafts are more prominent in the simulations than in the observations at IWC > 0.01 g m^{-3}, which is consistent with the comparisons in Figures 5 and 7. At this IWC range, all the simulations show larger increases in the frequencies of ISS ≥ 20% from near zero to ~0.3 as w increases from 0 to 3 m s^{-1}, while the observations show smaller increases in ISS frequencies (from ~0.1 to ~0.2). In addition, when w is above 3 m s^{-1}, all of the simulations show larger frequencies of ISS ≥ 20% than those in the observations, while they also show lower ISS frequencies in weaker updrafts and downdrafts (w < 0.5 m s^{-1}). For weaker updrafts and downdrafts, most of the simulated ISS is below 10% (Figure 9, first column), while only Morrison and Morrison-125% allow ISS ≥ 10% in strong downdrafts (w < -2 m s^{-1}). Thompson-aerosol is the only scheme that shows ISS frequencies greater than 0.1 at the lower IWC (<0.01 g m^{-3}), since more ice crystals with higher IWC are likely generated due to the Cooper parameterization in the other schemes.

Simulations also show stronger correlations between ISS and Nc than observations at Nc>100 L^{-1} (Figure 10), which is similar to those shown at IWC > 0.01 g m^{-3}. In addition, a lack of ISS occurrences at w < 0.5 m s^{-1} is shown in all the simulations at ISS ≥ 10%, except for Morrison-125%. One feature that is shown in Figure 10 but not in Figure 9 is that Thompson-aerosol has a peak ISS frequency at Nc around 0.1 L^{-1}, likely due to the predicted heterogeneous IN number concentration by the Phillips et al. (2008) parameterization.

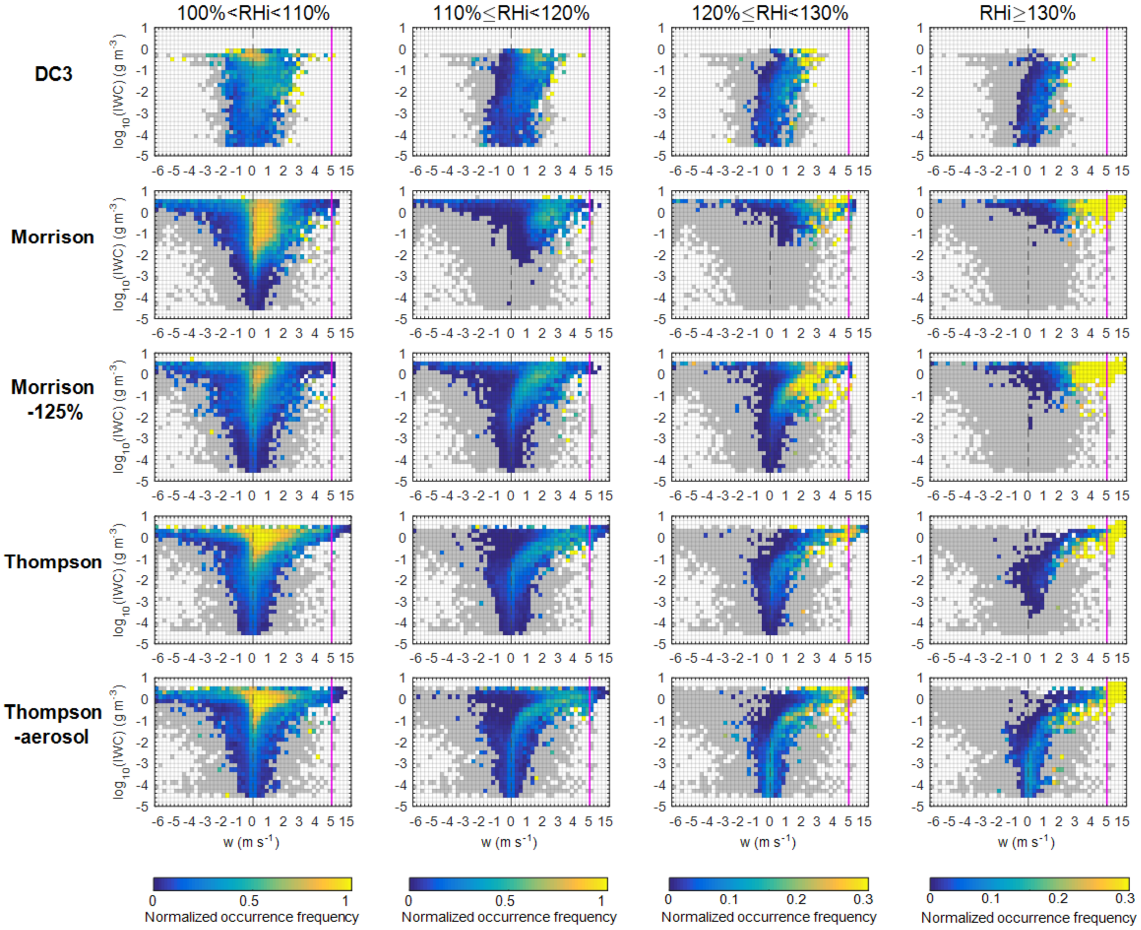

Figure 9. Normalized occurrence frequencies of ISS in relation to various magnitudes of w, controlling for IWC on the y axis. The four columns show analyses at four different ISS intervals. Occurrence frequencies of ISS are calculated by normalizing the ISS occurrences at each w and IWC bin with the total number of occurrences of all RHi in that bin. We note that two different bin sizes of w are used here: w is binned by 0.25 m s^{-1} for w < 5 m s^{-1} and by 2.5 m s^{-1} for w > 5 m s^{-1} (the maroon line highlights the transition between the two bin sizes). When w is below -6 m s^{-1} or greater than 15 m s^{-1}, these strong downdrafts/updrafts are grouped into the minimum and maximum w bins, respectively. The dashed line differentiates between updrafts and downdrafts. The gray colors represent the background of all RHi being observed or simulated.

To examine the effects of potential ice particle shattering, results with restricted Nc values (excluding ice particles smaller than 100 μm) are also provided. Similar occurrence frequency distributions of ISS are shown in the observations with and without such restriction.

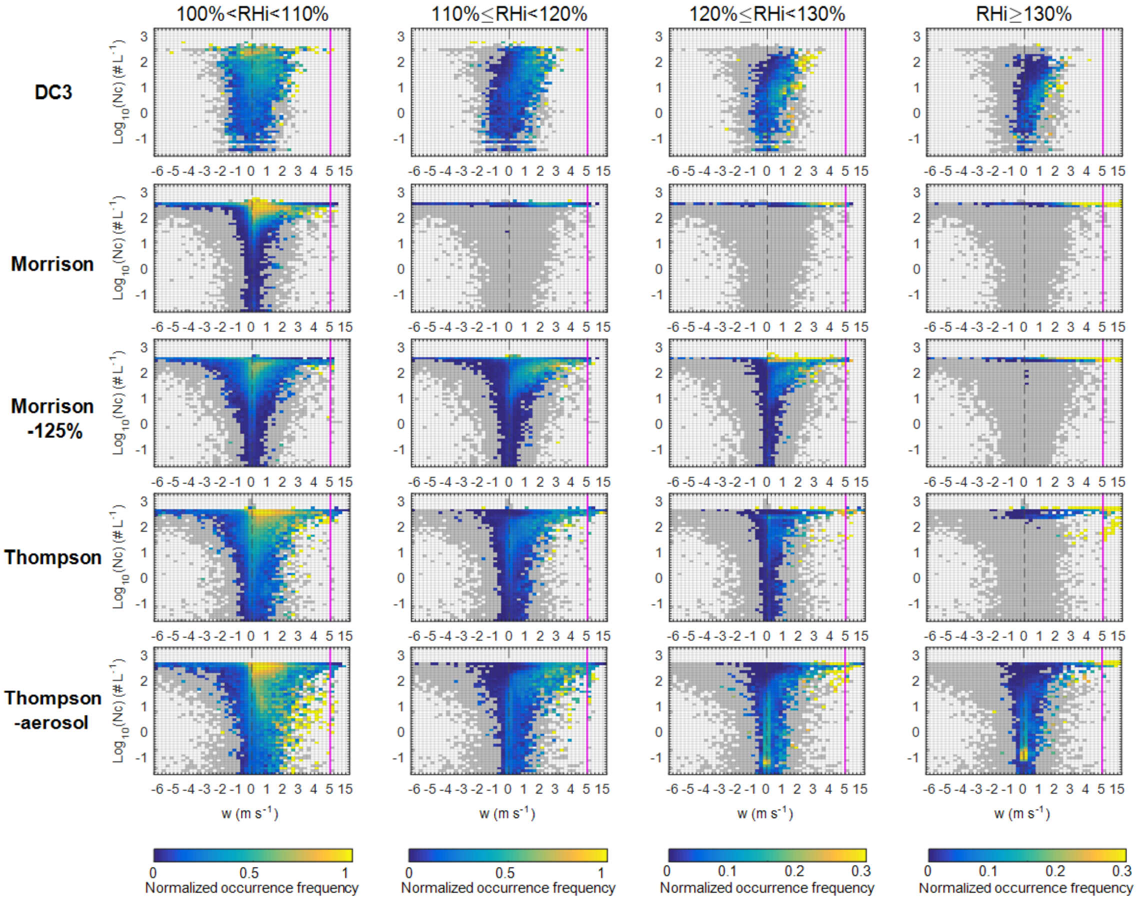

Figure 10. Normalized occurrence frequencies of ISS in relation to various magnitudes of w, controlling for Nc on the y axis. Same as Figure 9 except controlling for Nc when analyzing the correlations between ISS occurrence frequencies and w.

2.3.6 The influences of different sampling methods, time outputs, and case studies

To examine the sensitivity of the relationship between ISS and w to the spatial/temporal sampling method, we analyze the normalized occurrence frequencies of ISS for the WRF gridded data collocated with the observations during the 19 May flight (Figure 11, top three rows). WRF gridded data were selected within certain spatial ranges of the in situ observations in latitude and longitude (i.e., ±0.5°, ±1.5°, and ±3.0°) and within a time window (±30 min). Six-hourly outputs were used for the collocated comparisons from 19 May, 2100 UTC, to 20 May, 0200 UTC. The results are shown for the Thompson-aerosol aware simulation, while other microphysics schemes show similar consistency when conducting the collocated comparisons. In addition, to examine whether the correlations between ISS and w vary with the time evolution of the convective system as well as with different convective events, the normalized occurrence frequencies of ISS are analyzed for three combined time outputs during a separate convective episode on 11–12 June 2012 (Figure 11, bottom four rows). The domain of the 11–12 June 2012 simulations also coincided with flight observations during the DC3 campaign. This day was marked by isolated thunderstorms over Missouri/Arkansas and a mesoscale convective system over Alabama, both of which were sampled by the GV aircraft.

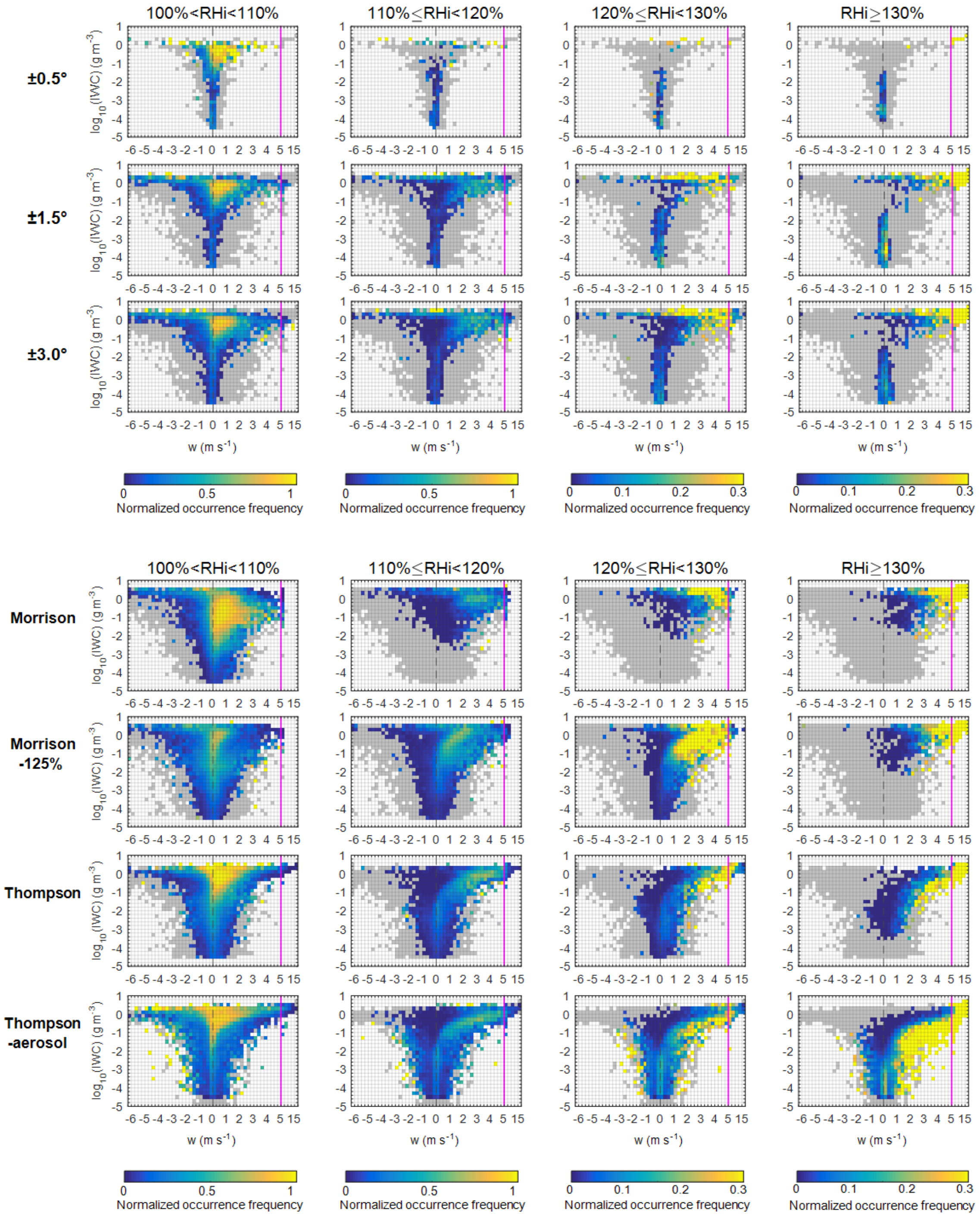

Figure 11. Similar to Figure 9 except for gridded data from Thompson-aerosol collocated with the 19 May GV aircraft observations within ±0.5°, ±1.5°, and ±3.0° in latitude and longitude and within ±30 min (top three rows); a different time period, i.e., during 11–12 June 2012 consisting of three merged time outputs (1600, 2000, and 0000 UTC) (bottom four rows).

Overall, the two main differences between observations and simulations in the 19–20 May 2012 case (Figure 9) are captured in these two sensitivity tests shown in Figure 11. That is, (1) a stronger gradient in ISS frequencies is shown in the simulations than observations at IWC > 0.01 g m^{-3} and (2) a lack of ISS occurrences at $w < 0.5$ m s^{-1} is shown in the simulations. However, Thompson-aerosol is still the only scheme that captures the ISS frequencies > 0.1 associated with lower IWC values (1 m s^{-1} than that in the 19–20 May 2012 case. These results indicate that the comparisons between observations and simulations on the correlations between ISS occurrence frequencies and w do not vary significantly by convective events arising from different synoptic/mesoscale forcings or by using more restrictive sampling methods.

The normalized frequency distributions of ISS are further compared among different time outputs of the same convective episode. Analyses on the four individual time outputs used in the composite data sets of the 19–20 May 2012 case are shown for Morrison and Thompson (Figure 12).

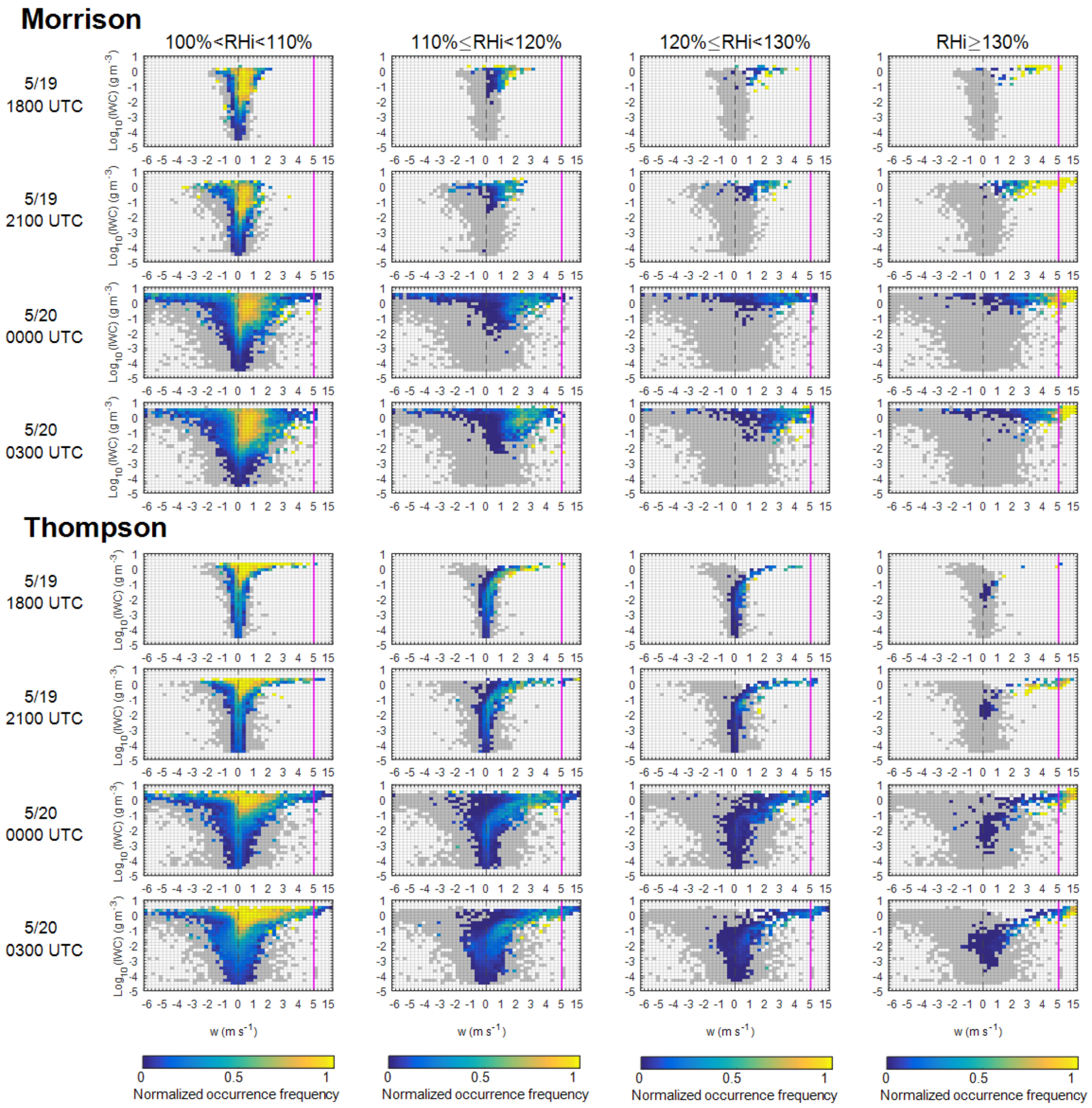

Figure 12. Similar to Figure 9 but shows four individual time outputs of WRF simulations at 1800, 2100, 0000, 0300 UTC during 19–20 May 2012. Results of the Morrison and Thompson simulations are shown in the top and bottom plots, respectively.

There is a noticeable evolution of the normalized frequencies of ISS from 1800 UTC to 0300 UTC, namely, the full range of w distributions increases from ±1 m s^{-1} to greater than ±6 m s^{-1} at ISS conditions. Nevertheless, the sharp gradient in ISS frequencies between stronger updrafts (w > 0.5 m s^{-1}) and weaker updrafts is still visible among individual time steps. In addition, the lack of ISS associated with $w < 0.5$ m s^{-1} at high IWC values (>0.01 g m^{-3}) is also consistently shown in these time outputs. These results indicate that even though the range of w varies among different time outputs, the overall distributions of ISS frequencies, as well as their correlations with w and IWC, are consistent regardless of the selection of time outputs for our analysis.

2.4 Discussion and Conclusions

WRF simulations with the Morrison et al. (2009), modified Morrison, Thompson et al. (2008), and Thompson and Eidhammer (2014) microphysics schemes captured both in-cloud and clear-sky ISS. The Cooper parameterization for ice crystal formation is included in the first three schemes but not in Thompson-aerosol. Including or excluding the Cooper parameterization, as well as changing the RHi thresholds for initiating the Cooper parameterization, has large impacts on our analysis of RHi, IWC, and Nc. For RHi distributions at temperature ≤ 40°C (Figure 2), the Cooper parameterization restricts the frequency and magnitude of ISS in simulations compared with the observations, which is likely due to the high number concentrations of ice particles being formed through this parameterization. By increasing the RHi threshold for the Cooper parameterization from the default 108% to 125% in Morrison-125%, a significant increase in the occurrences of RHi above 108% is shown. Additionally, the Cooper parameterization restricts the simulations from having lower IWC or lower Nc values at larger values of ISS. For example, Morrison does not have IWC < 0.01 g m^{-3} or Nc < 100 L^{-1} at ISS ≥ 8%. Other microphysics schemes that predict ice nucleation as a function of temperature may potentially yield similar discrepancies as produced via the Cooper parameterization. Thus, results from this study suggest that the Cooper parametrization, if included, should be initiated at higher RHi values (such as RHi ≥ 125%) at temperatures ≤ -40°C. Given the simplicity of the Cooper parameterization for more economical computations, adjusting the RHi threshold is found to be more effective for improving the simulations of ISS and ice nucleation compared with modifying the upper limit of

Nc. Thus, the Cooper parameterization with the adjustments recommended will still be valuable, and it does not involve the uncertainties of aerosol fields when using the Thompson-aerosol scheme. Based on these results, microphysics schemes are recommended to consider limiting ice nucleation at lower ISS even at low temperatures ≤ 40°C. These results are consistent with the previous remote sensing studies focusing on warmer conditions (> -40°C), suggesting that ice nucleation is limited when RHi is below water saturation (Ansmann et al. 2008; de Boer et al. 2011).

Comparisons between ISS and w at various IWC (Nc) ranges in the observations show a consistent positive correlation between probabilities of ISS and w (Figures 5 and 6), suggesting that higher w is generally required to generate and/or maintain the higher magnitudes of ISS. Such positive correlations between ISS probabilities and w are stronger when IWC or Nc increases, or when ISS magnitudes increase. In contrast, two types of ISS-w correlations occur in the simulations: a positive correlation at IWC > 0.01 g m^{-3} (or Nc > 100 L^{-1}) and a negative correlation at lower IWC (or lower Nc). Although the simulations have a positive correlation between ISS probabilities and w at higher values of IWC or Nc, such correlations are much stronger in the simulations with differences in ISS probabilities up to 4 orders of magnitudes between weak and strong updrafts (i.e., 0.1–4 m s^{-1}). In comparison, the differences in observations are only up to 2 orders of magnitude. The stronger dependence of ISS probabilities on w in the simulations for generating and/or maintaining ISS at IWC > 0.01 g m^{-3} or Nc > 100 L^{-1} is consistently shown in a series of analyses (Figures 5–8) and is also evident by the large increases of ISS frequencies from weaker to stronger updrafts in Figures 9–12. As a result of this strong dependence on w in the simulations, a lack of ISS is associated with weaker updrafts and downdrafts (w < 0.5 m s^{-1}) at high IWC and Nc values in Figures 9–12.

The discrepancies in the correlations between ISS probabilities and w between the observations and WRF simulations may be due to several factors. For in-cloud ISS, it is possible that the relaxation rate of ISS (i.e., the time for the existing ice to deplete the available water vapor over ice saturation) may be excessive at higher IWC (or Nc), which would require stronger updrafts to enhance the magnitudes of RHi as the excess water vapor is rapidly depleted at relatively high IWC (or Nc). A series of previous studies have discussed the complex factors influencing the vapor deposition rates, including studies on the spherical particles (Korolev and Mazin 2003) and the nonspherical particles (Sheridan et al. 2009), as well as those on the uncertainties with regard to the kinetically limited growth (Harrington et al. 2009; Zhang and Harrington 2015). In addition, all the microphysics schemes in this study include homogeneous (and heterogeneous) freezing of cloud droplets and rain, which can affect ice concentrations and ISS relaxation rates below -40°C in and near deep convection. Thus, it is not just the representations of ice nucleation on aerosols (as opposed to activated cloud droplets/rain) that can lead to differences between simulations and observations, although large impacts are still seen in the ISS frequency and magnitude when modifying the Cooper parameterization threshold in Morrison-125%.

Another potential explanation for the different ISS-w correlations between the observations and simulations may be that the water vapor spatial heterogeneities on the cloud scale (~1 km) are not sufficiently resolved by the simulations. Water vapor spatial variabilities have been previously reported to be the dominant contributor to the variabilities of RHi for both clear-sky and in-cloud conditions compared with the spatial variabilities of temperature (Diao et al. 2014). One may argue that increasing the horizontal resolution of the WRF simulations would provide a better representation of the water vapor spatial heterogeneities. However, when reducing the horizontal grid spacing from 2.4 to 0.8 km, even though the ISS probabilities at various w ranges in all the simulations become closer to the observations at IWC > 0.01 g m^{-3} (or Nc > 100 L^{-1}), the simulations also show larger discrepancies compared with the observations for representing ISS probabilities at the lower ranges of IWC and Nc. More investigation, such as using a cloud-resolving model, is needed to examine if higher-resolution simulations could help to produce more comparable results to the observations.

We caution that there are several caveats with the current analysis, mainly due to various factors in addition to IWC and Nc that potentially influence ISS distributions, such as the evolution of ISS and ice crystal regions (Diao et al. 2013b). The analysis of ISS, IWC, and Nc in this study represents a composite data set that sampled cirrus clouds at various evolution stages (e.g., nucleation, growth, and sedimentation). We examined the correlations between ISS frequencies and w at various pressures and altitudes and found that these two factors have smaller impacts than those of IWC and Nc. Another potential impact on the formation of ISS is from the various scales of dynamical processes, including smaller-scale gravity waves and turbulence, and mesoscale to synoptic-scale dynamical conditions, such as frontal uplifting, mesoscale gravity waves, warm conveyor belts, and jet streams (Spichtinger et al. 2005a; Muhlbauer et al. 2014; Diao et al. 2015; Spichtinger et al. 2005b). Additional work is recommended to further distinguish how the relationship between ISS and vertical velocity is represented by different cloud microphysics schemes in global climate models, where vertical velocity fluctuations associated with mesoscale phenomenon are parameterized due to the subgrid scale (<100km) nature of these fluctuations, as well as in smaller-scale model simulations such as the WRF-large eddy simulations.

Chapter 3

Relative Humidity Distributions in Southern Ocean Clouds: Comparing In Situ Observations with CAM5 Simulations

3.1 Background: Southern Ocean Clouds

Clouds over the Southern Ocean are an essential component controlling the energy budget over the region. Climate models struggle at simulating the radiative fluxes in the Southern Ocean region (~50°–80°S), underestimating reflected shortwave radiation on the order of 10 W m^{-2} (Bodas-Salcedo et al. 2014; Li et al. 2013; Kay et al. 2012) This is in part because climate models as well as higher-resolution regional models often simulate lower cloud fraction (Trenberth and Fasullo 2010) and less supercooled liquid water (SLW, i.e., liquid water existing at temperatures below 0°C) than observed in the high southern latitudes (Lawson and Gettelman 2014; Huang et al. 2014; Kay et al. 2016; Bodas-Salcedo et al. 2016). Additional consideration must be taken for MPC by characterizing the partitioning as well as the degree of mixing between ice and liquid particles, which can both substantially alter the radiation budget (Sun and Shine 1994).

The importance of local processes (relative to large scale processes, e.g., cyclonic activity) has been highlighted in previous studies. Climate models have difficulties capturing low-level clouds in the cold sector of midlatitude cyclones, which is potentially due to the observed prevalence of boundary layer clouds in these regions commonly associated with large-scale subsidence (Govekar et al. 2014; Bodas-Salcedo et al. 2014). The persistence of low and mid-level MPC in regions of large-scale subsidence is unexpected since adiabatic descent of air results in a warming process that reduces RH, and SLW is a microphysically unstable phase compared with the ice phase at temperatures below 0°C. Commonly referred to as the Wegener-Bergeron-Findeison process (WBF), ice particles will grow at the expense of neighboring liquid droplets due to differences in the equilibrium saturation vapor pressures of liquid and ice (e.g., Pruppacher and Klett 1996)). For the WBF process to occur, the local RH must be between the saturation vapor pressures of liquid and ice.

Validating simulated cloud properties and processes within climate models is crucial as many uncertainties still remain in predicting climate time scales of cloud feedbacks (e.g., Gettelman and Sherwood 2016). Global cloud feedbacks are often believed to be negative with surface warming, as surface heating will replace ice clouds with thicker liquid clouds (Mitchell et al. 1989). However, adjusting the parameterized phase partitioning of liquid and ice alone results in both positive and negative feedbacks globally when introducing surface temperature perturbations, relating to elementary cloud radiative forcings (Li and Le Treut 1992). Tan et al. (2016) constrained global climate model simulations using satellite observations and found an increase in equilibrium climate sensitivity of 1.3°C with a doubling of CO_2, resulting from a weakened positive cloud-phase feedback. Frey and Kay (2017) similarly found reduced negative cloud feedbacks over the Southern Ocean when simulating sufficient amounts of SLW to produce comparable shortwave radiation absorption as observed. McCoy et al. (2014) found comparable increases in upwelling shortwave radiation due to liquid replacing ice and increasing optical depths with a 1 K increase in the troposphere. Accurate representations of RH fields over the Southern Ocean are necessary in order to address these cloud feedback sensitivities, and observed RH tendencies may provide insight into cloud-scale processes responsible for the persistent cloud-regimes.

Due to a lack of in situ observations over the Southern Ocean, previous studies have utilized satellite-based RH data over the Southern Ocean (Lamquin et al. 2012; Gettelman et al. 2006; Kahn et al. 2009; Spichtinger et al. 2003b). Satellite-based RH data, such as from the NASA Atmospheric Infrared Sounder (AIRS) /Advanced Microwave Sounding Unit (AMSU) with a vertical resolution of 1–3 km and a horizontal resolution of 45×45 km, can be associated with large uncertainties in water vapor and temperature retrievals compared with in situ observations (Diao et al. 2013a). Although the satellite data provide useful information for climatological purposes, they cannot capture high-resolution RH distributions relevant to cloud-scale microphysical processes (e.g., the WBF process). In contrast, in situ observations can provide 1-second averaged RH measurements obtained from research aircraft, resulting in horizontal resolutions ranging from 100–250m. Ovarlez et al. (2002) analyzed in situ measurements of RH over the Southern Ocean, and found both high frequencies and magnitudes of ISS in midlatitude cirrus relative to cirrus sampled in the Northern Hemisphere. However, analyses mostly focused on regions relevant only for ice-only clouds (T<-40°C).

The purpose of this study is examine the distributions of cloud phases and RH during austral summer over the Southern Ocean based on in situ observations and simulations from the Community Atmosphere Model version 5 (CAM5). In situ observations are taken from the O_2/N_2 Ratio and CO_2 Airborne Southern Ocean Study (ORCAS) (Stephens et al. 2018), which took place during the austral summer. Local processes are relatively dominant at this time due to a seasonal decrease in cyclonic activity (Hoskins and Hodges 2005). Horizontal spatial averaging has been applied to the in situ observations to examine the effects of horizontal spatial resolution on the analysis results from the order of hundreds of meters to tens of kilometers. A series of model-observation comparisons have been conducted, including the cloud phase distributions at various temperatures, IWC and liquid water content (LWC) for three cloud phases, and RH distributions at in-cloud and clear-sky conditions. The prerequisite condition of ice particle formation – ice supersaturation (ISS = RHi - 100%) – has also been compared from -65° to 0°C between observations and simulations. These comparisons will help to shed more light on the reasons behind the challenges of accurately representing cloud thermodynamic phases and the amount of SLW over the Southern Ocean in climate model simulations.

3.2 Datasets and Experimental Set-up

3.2.1 In situ observations

This study uses 1 Hz airborne measurements from the NSF GV research aircraft during the ORCAS campaign. ORCAS took place from January 15 – February 28, 2016, sampling over the Southern Ocean from 30°S to 75°S and 92°W to 50°W. There were 18 flights in total, providing ~90 hours of flight time. Details on flight objectives and analyses can be found in Stephens et al. (2018). Observations in this study are restricted to temperatures <0°C to exclude warm cloud measurements (i.e., clouds with no ice or SLW). Temperature was measured using the Rosemount temperature probe, having an accuracy and precision of ±0.3 K and 0.01 K, respectively. Water vapor measurements are taken from the VCSEL hygrometer (Zondlo et al. 2010). The VCSEL hygrometer has an accuracy and precision of ~6% and ≤1%, respectively. Final data of water vapor mixing ratio and temperature were reported at 1 Hz. Two sets of RH data are calculated, i.e., RH with respect to liquid (RHliq) and ice (RHi), based on the equations in Murphy and Koop (2005) for saturation vapor pressures over liquid and ice, respectively. For temperatures relevant in this study, the uncertainties in RHi and RHliq range from 7.5%–6.5% to 10.4%–6.4% at -69°C to 0°C, respectively. Due to combined uncertainties from water vapor and temperature measurements, the observed RHliq greater than liquid saturation is set to be equal to 100.01% (processed for 7745 s of observations). Note that such restriction does not alter the number of occurrences for liquid or ice supersaturation.

Cloud particle measurements were made by the 2DC and the Cloud Droplet Probe (CDP). The CDP measures particles ranging from 2–50 μm, whereas the 2DC detects particles ranging from 62.5 to 1600 μm in diameter. We define in-cloud conditions as having either CDP measurements of number concentration greater than 3.16×10^{-2} cm^{-3} and derived bulk density greater than 3.98×10^{-4} g m^{-3} or 2DC measurements with at least one count (the minimum derived bulk density reported was 4.68×10^{-5} g m^{-3}). The rest of the measurements are defined as clear-sky conditions. The CDP thresholds are chosen in order to minimize the impacts of giant aerosols, which were determined by the relationships between number concentrations and bulk densities.

3.2.2 Global climate model simulations

Results from in situ observations are compared with two types of simulations from the Community Atmosphere Model version 5 (CAM5) model: the nudged simulations and the un-nudged simulations. The nudged CAM5 simulations (hereafter named as "CAM-collocated") were forced to represent meteorological conditions (temperature, pressure and 3-D wind speed) as described in Wu et al. (2017), with a spin-up time of 14 days. The gridded data from un-nudged CAM5 simulations (hereafter named as "CAM-domain") were initialized by the Global Forecast System (GFS) 6-hourly 0.5°×0.5° data and prescribed with climatological sea surface temperature and sea ice extent. The simulations were run with a 1-year spin-up period and provided output every six hours (00, 06, 12 and 18 UTC). When conducting comparisons on the statistical distributions of RHliq and RHi, a composite dataset of un-nudged CAM5 simulations is obtained by combining 18 model outputs collocated with the nearest flight times of the GV aircraft during the 18 research flights in the ORCAS campaign. CAM-domain is restricted to the horizontal regions (50°W to 92°W and 30°S to 75°S) and altitudes (pressure > 176.38 hPa) comparable to the ORCAS domain. Both simulations were run with a horizontal spatial resolution of 0.47°×0.63°, using 56 vertical levels with a pressure top of 30 hPa, and a timestep of 1800 s.

For analyses of cloud microphysical properties, the model output variables used are "LWC," "IWC," "NUMLIQ," and "NUMICE," all of which are grid box average quantities. When defining in-cloud conditions, either the value of LWC or IWC being greater than 4.68×10^{-5} g m^{-3}

is considered to be in-cloud condition, while the rest are defined as clear-sky condition. Such definition is consistent with the minimum detected value of CWC from the in situ observations. The calculation of RHi and RHliq is based on Goff and Gratch (1946) in the CAM5 simulations. Since the observations calculate saturation vapor pressures based on equations from Murphy and Koop (2005), this results in differences within ±0.3% for both RHi and RHliq values.

3.2.3. Spatial averaging of observations

One of the main challenges for comparing in situ observations and global climate model simulations is their differences in spatial resolution. To address this inherent problem, 1-Hz airborne observations were averaged over varying time intervals, i.e., 10 s, 25 s, 50 s, 100 s and 200 s. According to the GV aircraft true air speed that ranges from ~100 m s^{-1} to ~250 m s^{-1} from near surface to the upper troposphere and lower stratosphere, the spatial averaging results in horizontal resolutions of ~1 km – 20 km and ~2.5 km – 50 km, respectively. Such spatial averaging is mostly applied to the horizontal direction since the true air speed of the aircraft is significantly higher in the horizontal than that in the vertical direction. No spatial averaging was applied to CAM-collocated or CAM-domain.

Cloud fraction is derived from the airborne observations by calculating the ratio of 1-Hz in-cloud observations over the total number of 1-Hz data for a given interval of time. If more than 10% of a time interval (Δtime) reports missing data, that sample would be discarded. Temperature, RHi, RHliq, LWC, IWC, liquid and ice number concentrations (Nc_{liq} and Nc_{ice}, respectively) are averaged over the entire time interval, which correspond well with the grid-average variables from CAM5 output, such as IWC, LWC, NUMLIQ and NUMICE. A "moving average" method is applied for each 1-Hz sample by averaging between ±N seconds or between –N and N+1 seconds, where N equals to (Δtime-1)/2 or Δtime/2 for odd or even Δtime values, respectively.

3.3 Results

3.3.1 Definition of three cloud phases

LWC and IWC are derived solely from CDP and 2DC observations. Samples detected by CDP are considered liquid if the number concentration is greater than $10^{-0.5}$ cm^{-3}, otherwise CDP samples are considered ice. Imagery from the 2DC cloud probe reveal a high frequency of large supercooled liquid droplets, which requires further discrimination of 2DC data. If the maximum diameter of a particle detected by 2DC exceeds 212.5 µm, the 2DC samples are considered ice. To discriminate large droplets detected by 2DC, if the standard deviation of the particles' diameters is below 50 µm or the maximum particle size detected by the 2DC has a diameter less than 112.5 µm, the 2DC measurements are liquid. Otherwise, the 2DC measurements are considered ice. This method was found to correspond well with the 2DC imagery, which predominantly had only droplets when the liquid condition was met. Cloud phase is derived from observations and is defined by the mass fraction of LWC to the in-cloud condensed water content (CWC) similar to Korolev et al. (2003). A given cloud sample is considered ice phase at $LWC/CWC \leq 0.1$, mixed phase at $0.1<LWC/CWC<0.9$ and liquid phase at $LWC/CWC \geq 0.9$. This definition is applied to both observations and simulated data.

Figure 13 shows a portion of samples as observed by the GV aircraft. Fluctuating LWC and IWC results in spatially homogeneous (e.g., 17:39:30–17:40:30 UTC) and heterogeneous (17:53:30–17:54:00 UTC) distributions of cloud phase over relatively short time segments, as highlighted by cloud phase markers below the condensed cloud water quantities (third row from top). LWC from the KING hotwire probe, which determines LWC by the voltage required to melt SLW after freezing on a copper wire (King et al. 1978), is comparable to LWC from the proposed methodology. This study does not utilize LWC measured by the KING probe due to uncertainties detecting large droplets and noise associated with ice particles (e.g., Vidaurre et al. 2011; Baumgardner et al. 2017; Li et al. 2013; Biter et al. 1987).

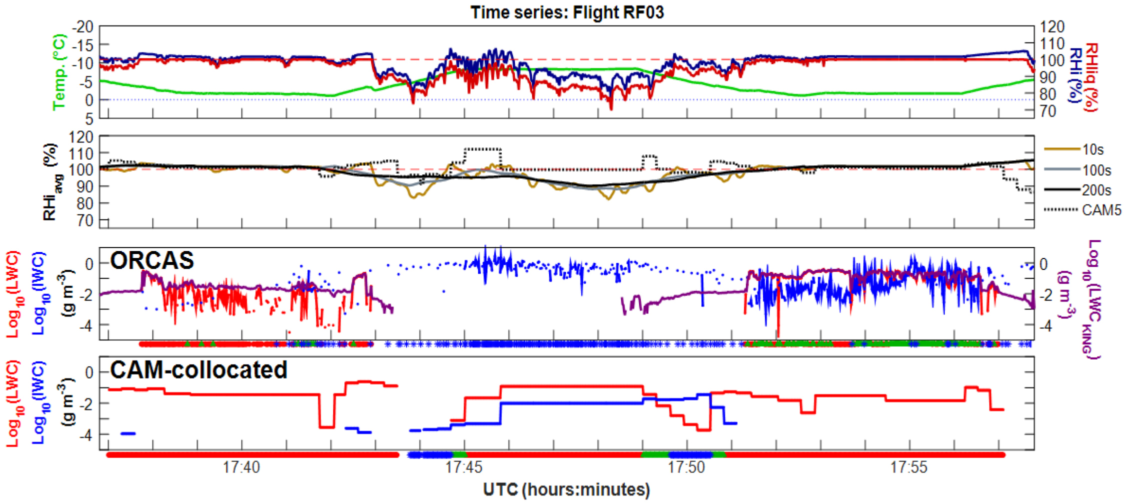

Figure 13. Time series showing a part of Research Flight 03 during ORCAS, including CAM-collocated results. Observations are output at 1 second for temperature, RHi, RHliq, IWC and LWC (rows 1&3) and averaged over different time intervals for RHi (row 2). Cloud phase as defined in Korolev et al. (2003) is shown by the markers underlying the corresponding panel of observed and simulated LWC and IWC. The red dashed lines in the top two rows are at saturation (RH=100%) and the dotted line in the top row is at 0°C.

The simulated liquid and ice partitioning result in more homogeneous distributions of cloud phase, failing to capture observed cloud phase heterogeneities (17:52:00–17:57:00 UTC). RHi averaged over different time intervals (10 s, 100 s and 200 s) roughly correspond with simulated RHi, albeit CAM-collocated produces liquid and ice at ice saturation within an observed ice-only region having subsaturated conditions (17:45:00–17:50:00 UTC). This scenario may be commonplace, and will be discussed further as evidenced by greater frequencies of observed subsaturation in ice-only conditions.

3.3.2 Cloud phase frequencies and characteristics

Examining how observations and simulations apportion IWC and LWC, the frequency of different LWC/CWC ranges is provided in Figure 14.

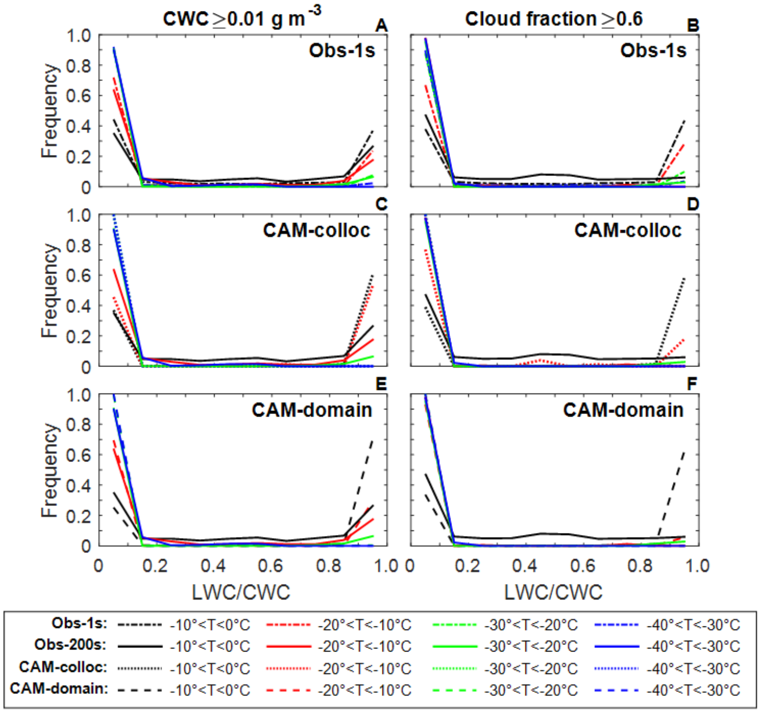

Figure 14. Occurrence frequencies of LWC/CWC for Obs-1s (A&B), Obs-200s averaged observations (all three panels; solid line), CAM-collocated (C&D) and CAM-domain (E&F). Obs-1s uses cloud fraction calculations over 10 second intervals (B). Occurrence percentages are rounded to the nearest integer.

The frequency of LWC/CWC are shown at 10°C intervals from -40–0°C, where ice and liquid can exist indefinitely given steady-state conditions. Results are controlled by CWC≥0.01 g m^{-3} (left column) and cloud fraction≥0.6 (right column). The number of samples for varying spatially averaged observational datasets as well as the different simulations are provided in Table 1, which similarly correspond CWC and cloud fraction restrictions as in Figure 14.

Table 1. The number of samples for different cloud phases as defined by Korolev et al. (2003). Results are shown for Obs-1s, Obs-200s, CAM-collocated and CAM-domain. The percentage frequency of each phase is provided in the parenthesis. Percentages are rounded to the nearest integer.

		CWC≥0.01 g m^{-3}			**Cloud fraction≥0.6**		
Dataset	**Temperature**	**Liquid**	**Mixed**	**Ice**	**Liquid**	**Mixed**	**Ice**
Obs-1s	**-10° to 0°C**	3098 (37%)	1587 (19%)	3726 (44%)	3825 (44%)	1628 (19%)	3329 (38%)
	-20° to -10°C	674 (24%)	131 (5%)	2056 (72%)	763 (28%)	131 (5%)	1800 (67%)
	-30° to -20°C	245 (7%)	74 (2%)	2950 (90%)	297 (10%)	74 (2%)	2641 (88%)
	-40° to -30°C	39 (2%)	100 (6%)	1599 (93%)	58 (4%)	111 (7%)	1471 (90%)
Obs-200s	**-10° to 0°C**	4507 (26%)	6533 (38%)	6017 (35%)	400 (6%)	3113 (47%)	3174 (47%)
	-20° to -10°C	1017 (17%)	1076 (19%)	3723 (64%)	0 (0%)	40 (2%)	1995 (98%)
	-30° to -20°C	359 (6%)	152 (3%)	5093 (91%)	79 (3%)	42 (2%)	2651 (96%)
	-40° to -30°C	0 (0%)	267 (11%)	2501 (89%)	0 (0%)	26 (2%)	1133 (98%)
CAM-colloc	**-10° to 0°C**	6599 (60%)	289 (3%)	4028 (37%)	4042 (59%)	173 (3%)	2689 (39%)
	-20° to -10°C	705 (53%)	18 (1%)	604 (46%)	700 (18%)	205 (5%)	2995 (77%)
	-30° to -20°C	0 (0%)	0 (0%)	978 (100%)	0 (0%)	0 (0%)	3315 (100%)
	-40° to 30°C	0 (0%)	0 (0%)	292 (100%)	0 (0%)	0 (0%)	2890 (100%)
CAM-domain	**-10° to 0°C**	112293 (70%)	6735 (4%)	40321 (25%)	84882 (63%)	4802 (4%)	45661 (34%)
	-20° to -10°C	5404 (29%)	195 (1%)	12793 (70%)	5564 (6%)	1236 (1%)	92236 (93%)
	-30° to -20°C	66 (1%)	3 (<1%)	12459 (99%)	28 (<1%)	32 (<1%)	72318 (100%)
	-40° to -30°C	0 (0%)	0 (0%)	10558 (100%)	0 (0%)	0 (0%)	54960 (100%)

Obs-1s, Obs-200s, CAM-collocated and CAM-domain all show decreasing frequencies of LWC/CWC<0.9 and increasing frequencies of LWC/CWC<0.1 with decreasing temperature, consistent with increasing frequencies of ice at lower temperatures. Obs-1s reveal similar distributions of cloud phase occurrence frequencies as shown in Korolev et al. (2017), which used Nevzorov measurements taken within frontal systems from Korolev et al. (2003) and updated them using post-processing methods from Korolev et al. (2013). Focusing on the CWC≥0.01 g m^{-3} condition, which is used in both studies, the datasets sampled approximately equal distributions of liquid-only and ice-only conditions (LWC/CWC≥0.9 and LWC/CWC≤0.1, respectively) from -10°–0°C. The liquid and ice phases each account for ~40% of the total number of occurrences. The number of liquid-only cases from -20° to -10°C is slightly larger in the ORCAS study (24%) relative to Korolev et al. (2017) (<20%).

From -10°–0°C, spatially averaged observations (Obs-200s) have approximately half the number of liquid phase samples and twice the number of mixed phase samples (0.1<LWC/CWC<0.9) as Obs-1s. This may be the result of averaging over spatially heterogeneous distributions of cloud phase. An exception is seen for the number of liquid phase samples using the cloud fraction threshold, which approximately decreases by a factor of 7 (44% for Obs-1s; 6% for Obs-200s). This is expected since the primary flight objective of ORCAS was to sample vertical profiles of various chemical species (e.g., O_2 and N_2), which resulted in the GV aircraft flying in and out of the long-lived boundary layer cloud regimes with minimal in-cloud residence times. Thus, many of the boundary layer clouds sampled aren't captured for Obs-200s as 60% of the observations must meet the 1 second in-cloud condition.

Relative to the observations, simulations have significantly lower frequencies of mixed-phase samples meeting the Korolev et al. (2003) definition. Interestingly, the simulations capture significantly more liquid-only cases relative to the observations. CAM-collocated produces liquid-only clouds over 50% of the time for the CWC ≥ 0.01 g m^{-3} condition from -20°–0°C. This is somewhat unexpected since climate models, including CAM5, have been reported to underestimate SLW and overproduce ice at temperatures relevant for mixed-phase conditions (e.g., Komurcu et al. 2014; Cesana et al. 2015). The apparent disparity of liquid-only and mixed-phase conditions may result in completely different simulated cloud processes from those actually occurring in the region.

Local RH measurements combined with observed LWC, IWC, Nc_{liq} and Nc_{ice} are required to further theoretical understandings of long-lived MPC regimes. In addition, climate models often fail to adequately capture mixed-phase conditions, as CWC is often parameterized to partition liquid and ice according to temperature. CAM5 utilizes a double moment cloud microphysics scheme with separate prognostic variables for both liquid and ice (Morrison and Gettelman 2008), which should allow for the simulations to capture a wide range of variability for relevant cloud processes. Thus, it is important to examine CWC and number concentration characteristics in conjunction with RH, and necessary to control for phase partitioning between the datasets.

Figure 15 shows observed averages of LWC, IWC, Nc_{liq} and Nc_{ice} at 5°C intervals. Quantities are initially scaled by base-10 logarithmic functions prior to averaging. Averaged quantities are shown for respective cloud phases from -40–0°C. Relative to spatially averaged observations, Obs-1s generally produce greater averaged quantities by 1–2 orders of magnitude, which is expected since spatial averages will include clear-sky conditions when cloud fraction<1.

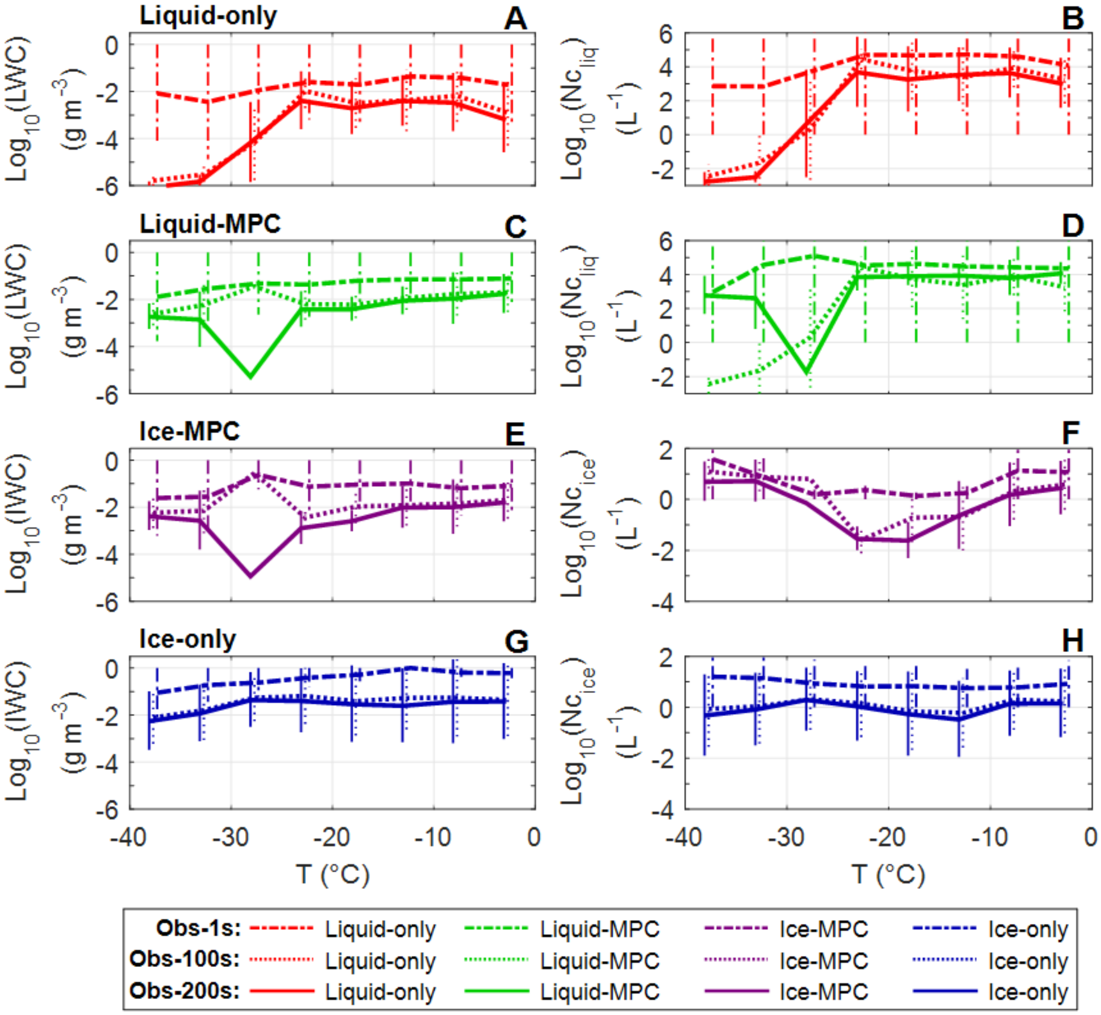

Figure 15. Average LWC, IWC, Nc$_{liq}$ and Nc$_{ice}$ for Obs-1s, Obs-100s and Obs-200s. Results are restricted to different cloud phases. Average values are shown by horizontal lines with bars representing standard deviation. Results are binned at 5°C intervals.

Trends in the averaged quantities with temperature are generally similar between Obs-1s and spatially averaged observations. LWC and IWC generally decrease with decreasing temperature independent of cloud phase. Average LWC is generally lower for liquid-only conditions compared with mixed-phase conditions, whereas average IWC is generally greater in ice-only conditions compared with mixed-phase conditions. Nc$_{liq}$ are fairly constant at temperatures

>-25°C, whereas Nc$_{ice}$ vary depending cloud phase. The observational datasets mostly differ at temperatures <-25°C, where average LWC and Nc$_{liq}$ dramatically decrease for Obs-100s and Obs-200s (Figure 15A,B,D). This may be a consequence of small sample sizes for the liquid and mixed-phase conditions from -40°C to -20°C.

Figure 16 shows averaged IWC, LWC, Nc$_{liq}$ and Nc$_{ice}$ for the simulations overlapped with Obs-200s.

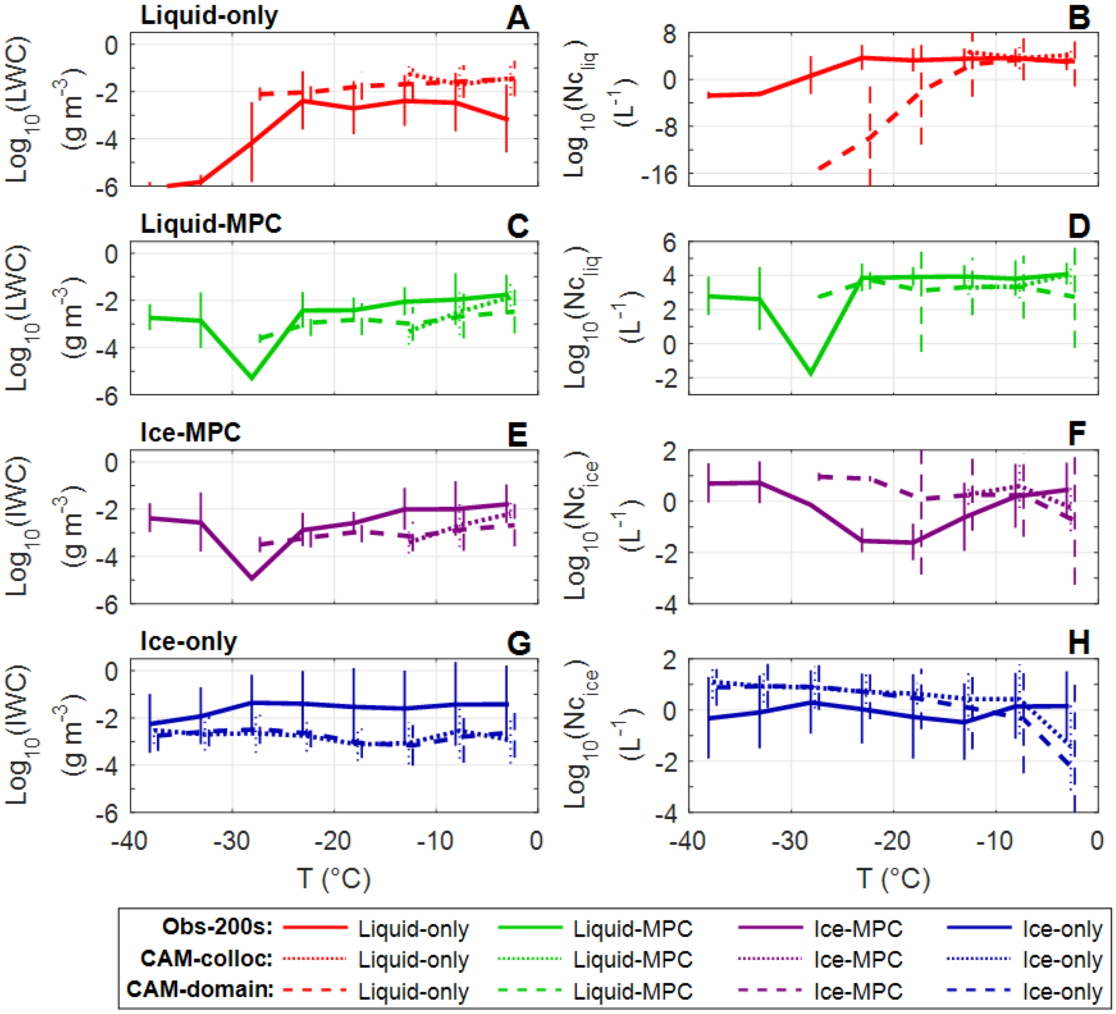

Figure 16. Average LWC, IWC, Nc$_{liq}$ and Nc$_{ice}$ for Obs-200s, CAM-collocated and CAM-domain. Results are restricted to different cloud phases. Average values are shown by horizontal lines with bars representing standard deviation. Results are binned at 5°C intervals.

Similar trends are seen for simulated quantities relative to the observations, namely, decreasing LWC and IWC with temperature (Figure 16A,C,E), and fairly constant Nc_{liq} at relatively warmer temperatures (>-15°C; Figure 16B&D). Averaged quantities are very similar amongst CAM-collocated and CAM-domain, never differing by more than ~0.5 orders of magnitude for any of the results. Simulated average LWC in liquid-only conditions are about an order of magnitude greater than Obs-200s, but comparable to averages from Obs-1s at 0.01–0.1 g m^{-3} (Figure 15A). Nc_{liq} are comparable between Obs-200s and the simulations at relatively warmer temperatures (>-15°C). The most notable differences are observed for ice-phase quantities. For ice-only conditions, simulated IWC is ~2 orders of magnitude less than Obs-200s and ~3–4 orders of magnitude less than Obs-1s (Figure 15G). Simulated Nc_{ice} are ~1–2 orders of magnitude less than observations at temperatures >-5°C, and ~1 order of magnitude greater than Obs-200s at temperatures >-10°C. Very low IWC and high Nc_{ice} in simulations suggest unrealistically high number concentrations of small ice particles are produced in CAM5.

3.3.3 Relative humidity distributions

Concentration is shifted towards examining the distributions of RH, which are controlled by cloud fraction. Figure 17 shows PDFs of RHliq at varies cloud fraction ranges. CAM5 calculates liquid cloud fraction in part using RHliq and ice cloud fraction solely as a function of RHi (total cloud fraction is determined by assuming maximum overlap between the two), highlighting the need for high resolution observations of water vapor for model validation. Results include various spatial averages of observations shown by the solid lines, ranging from 10–200 seconds. Simulated results are shown for both CAM-collocated (dotted) and CAM-domain (dashed).

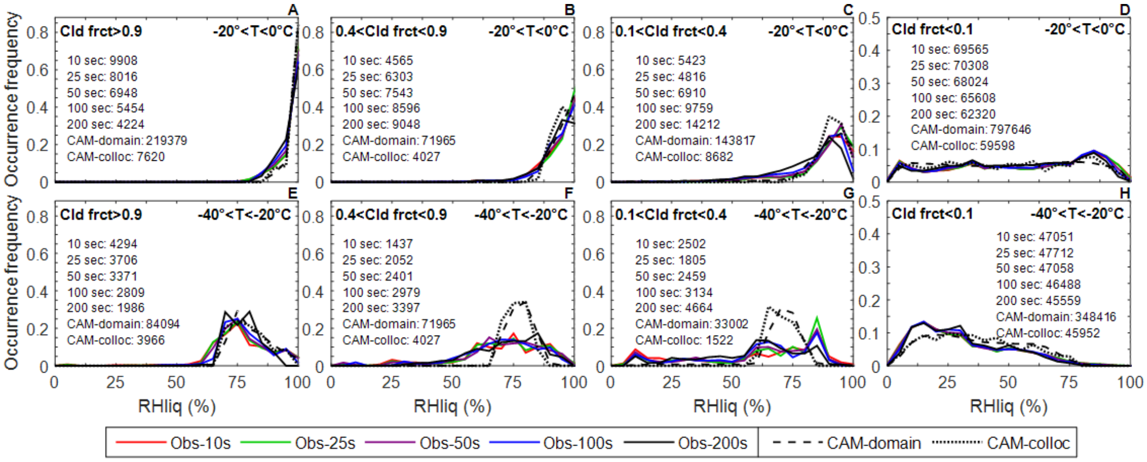

Figure 17. RHliq PDFs controlled by cloud fraction. Observations are averaged over different time intervals. Dotted and dashed lines are for CAM-collocated and CAM-domain, respectively. Results are binned by 5%, with the exception of 0%–2.5%. The number of samples are provided for each dataset within their respective panels.

RHliq distributions broaden with decreasing cloud fraction. At -20°–0°C, RHliq peaks at liquid saturation and shifts to ~85% as cloud fraction shifts from >0.9 to <0.1. Distributions are broader at -40°C to -20°C, and the peak frequency shifts from ~75% to 15% for observations. Spatially averaged observations have similar distributions at the different temperature and cloud fraction ranges. Likewise, simulations compare well with each other. At -20°–0°C, the observations and simulations have similar distributions. CAM-collocated similarly captures a mode of ~85% at cloud fraction<0.1. Many of the observations within -20°–0°C were taken at low altitudes (often below the boundary layer), suggesting CAM5 does a good job at simulating low-level water vapor fields. Differences between the observations and simulations are greatest at -40°C to -20°C and cloud fraction ranging from 0.1–0.9, characterized by broader distributions seen in the observations. Spatially averaged observations have a higher variability in the magnitude of RHliq.

Different condensed cloud water phases may skew RH distributions either towards liquid or ice saturation, assuming the majority of in-cloud samples were taken in steady-state conditions.

Because of this, varying occurrence frequencies of different cloud phases may impact the observed trends. To see how distributions may be impacted, Figure 18 provides RHi PDFs similarly constrained by cloud fraction.

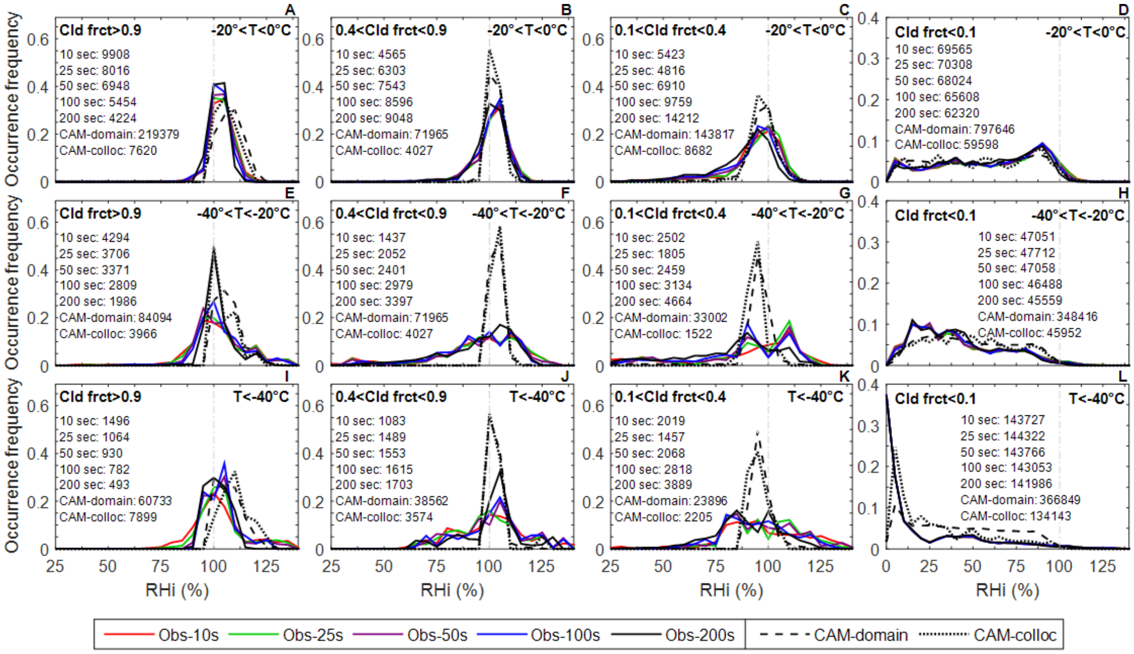

Figure 18. RHi PDFs controlled by cloud fraction. Same as Figure 17, except results are shown for RHi.

RHi distributions are also shown at temperatures <-40°C, where the ice phase is relevant. Compared to RHliq PDFs, the peak frequencies shift towards decreasing RHi with decreasing cloud fraction for simulations. However, the shift is much more pronounced for simulations, which have a peak frequency shift from RHi≥100% to ~90% as cloud fraction decreases to 0.1. Spatially averaged observations generally have distributions center at ±10% from ice saturation, and increasingly broader distributions as cloud fraction decreases. Results similarly capture narrower distributions for the simulations at colder temperatures (<-20°C) and cloud fraction ranging from 0.1–0.9. Both CAM5 simulations have sharp peaks within ±10% of ice saturation and do not capture the magnitudes of both ISS and subsaturation as observed. From -20°–0°C, the datasets similarly differ only for subsaturated conditions. At temperatures <-40°C, fewer subsaturated and more supersaturated samples are seen relative to -40°C to -20°C. At lower temperatures, where ice cloud fraction dominates in the contribution towards total cloud fraction, it is important to consider its dependence on RHi as well as a prescribed maximum and minimum humidity threshold. Simulations use the default threshold values (RHi_{max}=1.1; RHi_{min}=0.8). Adjusting these values may produce more comparable RHi distributions, whereby allowing for both greater frequencies and magnitudes of in-cloud ISS and subsaturation.

The greatest differences between observations and simulations were found at in-cloud conditions (cloud fraction>0.1) and temperatures <-20°C, coinciding with primarily ice-only conditions. To see whether RH discrepancies are phase dependent, Figure 19 provides RHliq CFDs controlled by cloud phase.

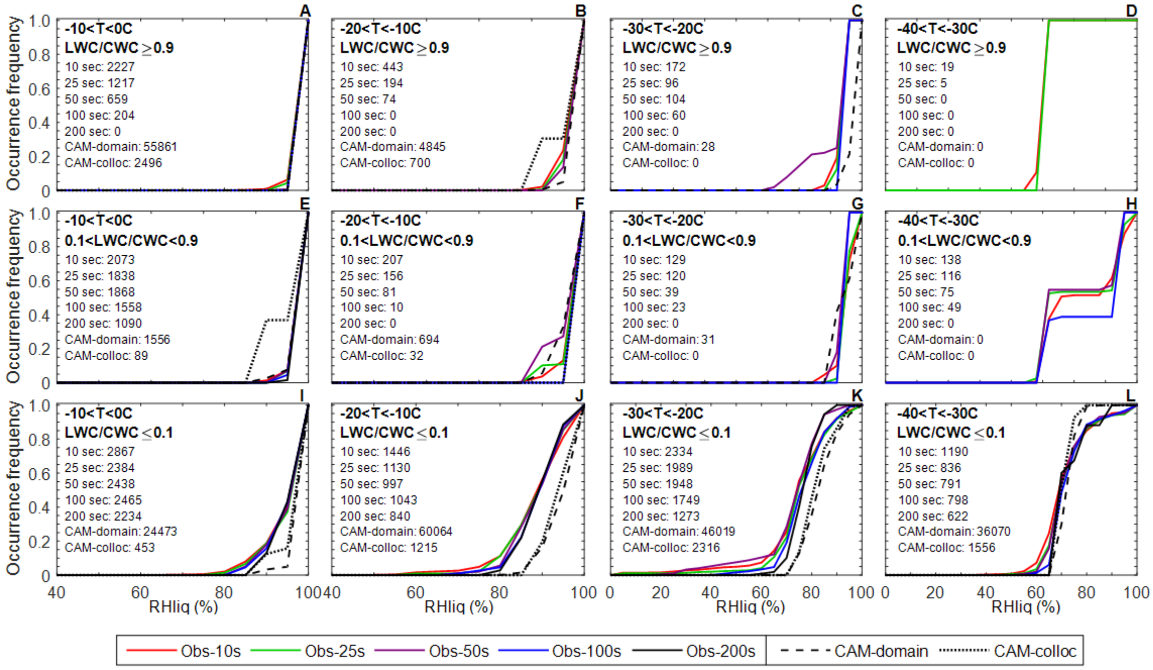

Figure 19. RHliq CFDs controlled by cloud phase. Observations are averaged over different time intervals. Dotted and dashed lines are for CAM-collocated and CAM-domain, respectively. Each sample has a cloud fraction ≥ 0.9. Results are binned by 5%, with the exception of 0%–2.5%. The number of samples are provided for each dataset within their respective panels.

Results are shown at 10°C intervals from -40°–0°C. Cloud fraction is restricted to ≥0.9 in order to minimize the number of clear-sky samples included in the spatial averages. The vast majority of samples for liquid and mixed-phase conditions occur at RHliq greater than 90% from -30°–0C°. Cumulative frequencies for the spatially averaged observations have at least ≥95% of the samples at RHliq>97.5% from -10°–0°C, ≥70% of the samples at RHliq>97.5% from -20° to -10°C, and ≥70% of the samples at RHliq>92.5% from -30° to -20°C. At -10°–0°C CAM-domain cumulative frequencies are near identical with observations (Figure 19A&E), and remarkably similar from -30°C to -10°C. Results are consistent with the theoretical understanding that MPC will have a steady state RH at liquid saturation (Korolev and Mazin 2003) and previous observations of local RHliq in both liquid and mixed-phase conditions which centered slightly below saturation as a result of sampling cloud holes (Korolev and Isaac 2006). The high frequency of liquid and mixed-phase conditions near liquid saturation to temperatures as low as -30°C suggests the methodology has sufficient success in capturing the existence of SLW. The greatest differences between the datasets are seen in ice-only conditions at all temperatures shown (Figure 19I–L). Both simulations underestimate subsaturated occurrences for all the ice-only conditions, with the greatest differences at temperatures >-30°C, illustrated by observations capturing ~40% more ice-only samples having RHliq<90% relative to the simulations at -20° to -10°C. At temperatures <-30°C, ~15% of observations have RHliq>80% whereas simulations don’t have any samples of RHliq>80%.

To see how the observations and simulations distribute subsaturated and supersaturated conditions with respect to ice, Figure 20 shows CFDs of RHi for separate cloud phases. Liquid-only and mixed-phase distributions of spatially averaged observations shift towards larger magnitudes of ISS with decreasing temperature, and are similarly in agreement with simulated distributions as seen in Figure 19A–C and 19E–G. Simulations similarly underestimate the number of subsaturated occurrences relative to observations, as seen in Figure 19I–L. At -10°–0°C the ice phase has ~60% of observations subsaturated, whereas CAM-collocated and CAM-domain are closer to ~25% and ~10%, respectively. At temperatures <-30°C, Obs-200s has similar cumulative frequencies as the simulations below ice saturation. However, the simulations don't capture RHi>~110%, which account for ~15% of all the spatially averaged observations.

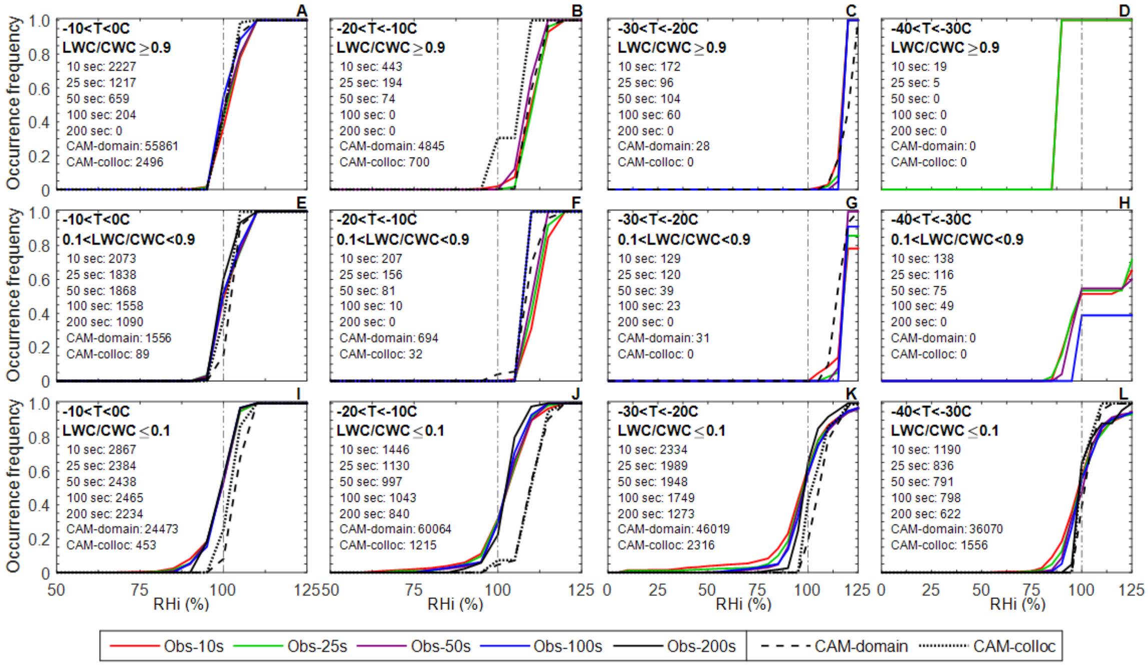

Figure 20. RHi CFDs controlled by cloud phase. Same as Figure 19, except results are shown for RHi.

Average simulated and observed IWC are within one order of magnitude at these lower temperatures, and vary substantially at relatively warmer temperatures (>-30°C; Figure 16G). Simulations characterized by low IWC and high Nc_{ice} from -30°–0°C (Figure 16G&H) combined with the under-simulated occurrences of subsaturation in ice-only conditions possibly suggest CAM5 is failing to capture a conceivably high frequency of ice sedimentation into underlying subsaturated layers over the Southern Ocean (as seen in Figure 13).

Deposition/sublimation resulting from ice sedimentation may result in significantly different distributions of moisture content vertically. To explore this, as well as the partitioning of subsaturated and supersaturated cases with respect to ice vertically, Figure 21 shows the occurrence frequencies of three cases: 1) clear-sky ISS, 2) in-cloud ISS, and 3) in-cloud non-ISS at temperatures < 0°C.

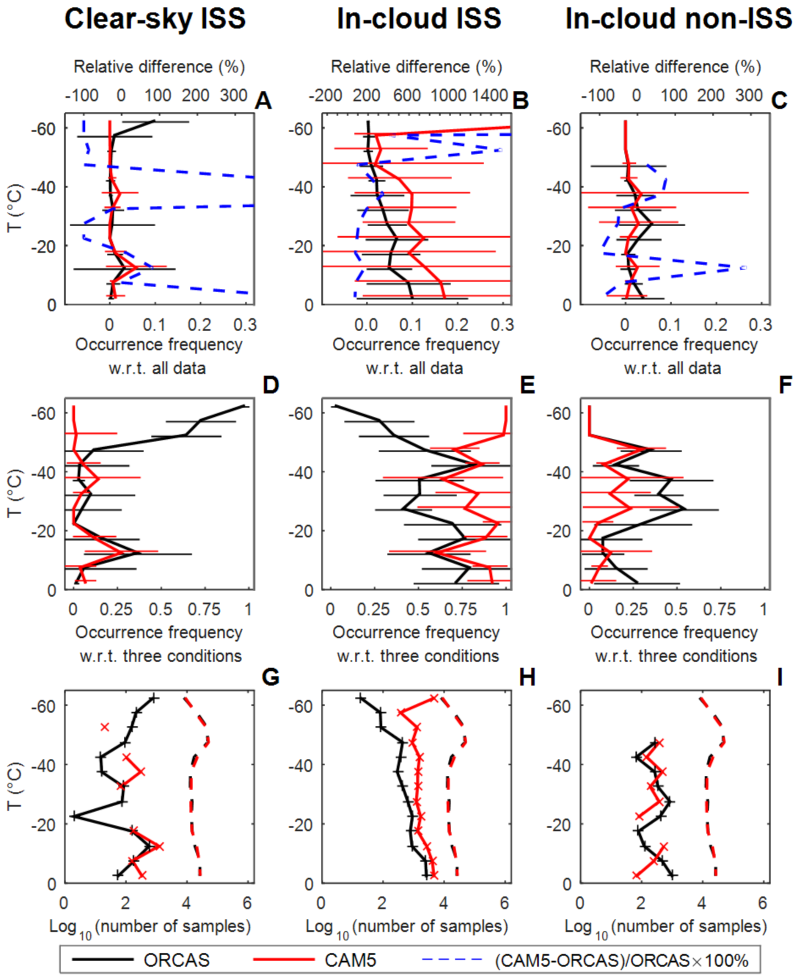

Figure 21. Vertical profiles of clear-sky ISS, in-cloud ISS and in-cloud non-ISS occurrence frequencies for Obs-200s and CAM-collocated, normalized by the total number of samples (top row) and the total number of clear-sky ISS and in-cloud samples (middle row) binned at 5°C intervals. The number of occurrences for each of the 3 cases (lines with markers) and total number of samples in each dataset (dashed lines) are in the bottom row. The blue dashed line (top row) shows the relative difference (in %, upper abscissa). Horizontal bars represent the corrected sample standard deviation among the 18 research flights. In-cloud cases are restricted to cloud fraction ≥ 0.6 and clear-sky cases have cloud fraction < 0.1.

Two types of occurrence frequencies are shown, i.e., frequencies normalized by all samples (Figure 21A–C), and relative frequency normalized by the total number of the aforementioned three cases (Figure 21D–F). Results are shown for Obs-200s and CAM-collocated. In-cloud and clear-sky conditions are defined as cloud fraction≥0.6 and cloud fraction<0.1, respectively. For clear-sky ISS conditions, results are strikingly similar between observations and CAM-collocated from -50°C–0°C. Both datasets similarly reveal an increase in frequency between -15°C to -10°C. However, the simulations underestimate the clear-sky ISS frequencies and overestimate the in-cloud ISS frequencies below -50°C (Figure 21A–B). Relative frequencies between the datasets increasingly differ as temperature decreases below -40°C (Figures 21D–F). This is seen by the majority of observed ISS samples as being clear-sky while the majority of simulated ISS grid points are in-cloud, most notably below -60°C where CAM-collocated produces cirrus (in-cloud ISS) more frequently than observed by two orders of magnitude. These differences may be caused by excessive ice production at lower temperatures in CAM5, or a lack of clear-sky ISS segments at the sub-grid scale (Wu et al. 2017; Diao et al. 2014).

Focusing on temperatures >-40°C, differences between the datasets appear exclusively for the in-cloud profiles. The major differences in relative frequency occur at -10°–0°C and -40°C to -20°C (Figure 21E&F). Differences at the relatively warmer temperatures (>-20°C) correspond with the greater occurrence frequency of simulated liquid-only samples relative to observations, seen by the greater frequency of in-cloud ISS. However, the number of liquid-only observations is dramatically reduced as a consequence of the cloud fraction threshold used, due to the aircraft puncturing boundary layer clouds for short durations. Differences at the relatively colder temperatures (<-20°C) correspond with the greater number of observed subsaturated samples at this range, which was shown to correspond with ice-only samples.

An overview of the RHi distributions at various temperatures is shown in Figure 22, where the differences of normalized RHi frequency between Obs-200s and CAM-domain are shown for each 1°C×5% bin. The RHi frequencies are calculated for each 1°C interval. Results are shown for cloud fraction ranges <0.1, 0.1–0.9 and ≥0.9. For cloud fraction≥0.9, Obs-200s has samples centered on ice saturation, where the greatest ISS doesn't exceed 25% (RHi=125%).

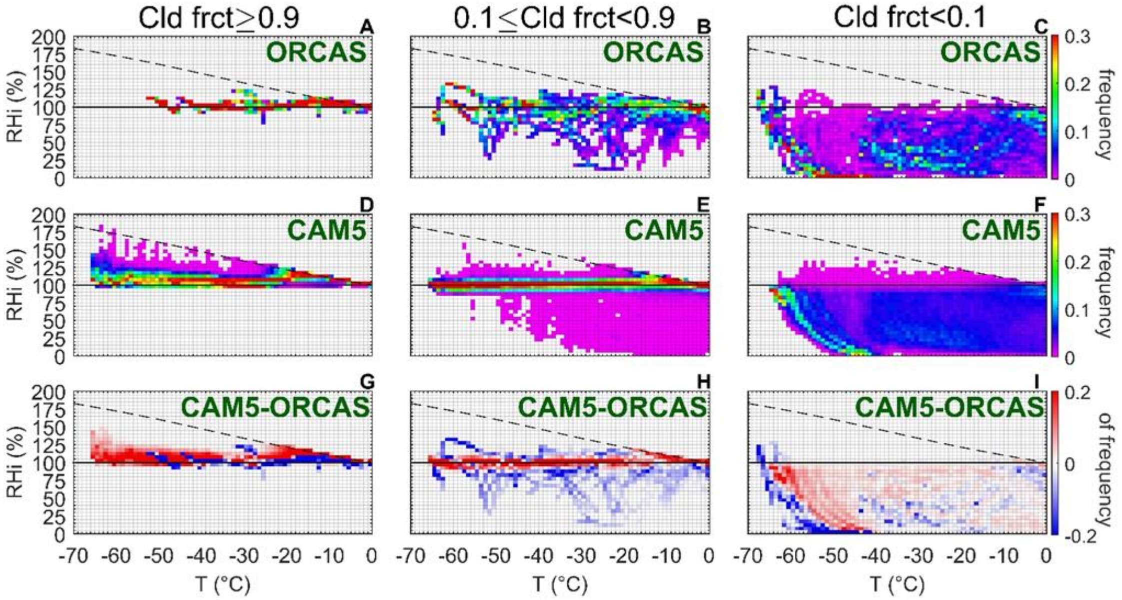

Figure 22. RHi frequency distributions with respect to temperature for Obs-200s (A–C), CAM-domain (D–F) and their differences (CAM-domain – Obs-200s; G–H). Occurrence frequencies are normalized by temperature at 1°C intervals. The solid and dashed lines are saturation with respect to ice and liquid, respectively.

CAM-domain has larger magnitudes of ISS, but there are so few cases that differences between the dataset are indiscernible at high ISS (Figure 22G). In contrast, a greater number of subsaturated and supersaturated samples are seen at cloud fraction ranging from 0.1–0.9. Consistent with in-cloud RH PDFs controlled by cloud fraction (Figures 16 and 17), a narrower RHi distribution at in-cloud conditions is seen in CAM5 simulations compared with the observations, exhibited by overestimates of in-cloud RHi frequencies between 95% and 110% at temperatures < -20°C. Underestimations of the simulated in-cloud RHi frequencies are seen with a sharp cutoff below 95%, again highlighting the minimal number of subsaturated in-cloud cases.

3.4 Conclusions and implications for climate simulations over the Southern Ocean

In this study we compare in situ airborne measurements of RHi and RHliq observed over the Southern Ocean (50°W to 92°W and 30°S to 75°S) with simulated RHi and RHliq from CAM5 simulations, respectively. Airborne measurements are averaged over varying time intervals in order to produce observational datasets having reduced spatial scale differences with gridded data. Observations are compared with two sets of CAM5 simulations, one containing all gridded data within the region sampled for the duration of ORCAS (CAM-domain) and another simulation with gridded data collocated with the ORCAS flight tracks (CAM-collocated). The two simulations primarily produce comparable results, suggesting statistical significance when comparing highly localized in situ observations with simulations over a significant portion of the Southern Ocean. For observations, scaling in situ measurements on the order of minutes often results in comparable distributions of RH averaged on the order of seconds. Thus, averaging over tens of kilometers, which consequentially results in averaging over varying steady- and quasi-steady states, has minimal impact on the scaling method. Overall, results suggest a comparability between the high resolution aircraft observations and coarsely gridded climate model simulations. Analyses of RH are controlled by temperature, cloud fraction and cloud phase. Comparisons controlling for CWC were tested and found to produce disparate results. This is because averaging CWC, which varies by several orders of magnitude over a given time interval, produces a large variance in the number of in-cloud conditions met.

Results suggest that CAM5 adequately captures the observed moisture fields within clear-sky conditions at relatively low altitudes (>-20°C), exhibited by near-identical clear-sky RH frequency distributions. A mode at RHliq of ~85% reveals relatively moist conditions at low altitudes. An abundance of low level moisture has been noted in previous studies of Arctic clouds, which helps to explain long-lived cloud regimes in spite of (1) the microphysical instability of commonly observed MPC, (2) their coexistence in regions of large scale subsidence and (3) commonly observed ice precipitation (Morrison et al., 2011 and sources within). Sources for the abundance of low-level moisture have been attributed to (1) surface sourced moisture from a surface-coupled atmospheric profile and (2) near cloud-top entrainment of overlying moisture inversions (Solomon et al. 2011; Morrison and Pinto 2006). In contrast to clear-sky conditions, in-cloud RH distributions can vary substantially between the datasets. Overall, observations produce much broader distributions of RH, characterized by greater magnitudes of subsaturation and ISS most notably at relatively colder temperatures (<-20°C) and cloud fraction ranging from 0.1–0.9. We note the potential for adjusting the RHi_{min} and RHi_{max} parameters in CAM5 used to diagnose ice cloud fraction, which is solely a function of RHi. However, observed cloud fraction < 0.4 having ISS>15% as well as cloud fraction > 0.9 having RHi<85% (Figure 2) in part casts doubt on the applicability of parameterizing ice cloud fraction solely as a function of RHi.

Cloud phase is determined by the mass ratio of liquid over the total condensed cloud mass (similar to Korolev et al. (2003)). Observed cloud phase frequencies correspond closely with those from Korolev et al. (2017), whereas CAM5 produces exceptionally few mixed-phase samples. Observations reveal high occurrence frequencies of SLW from -20°–0°C (Figure 14; left column), consistent with previous studies that frequently reported SLW in this region (Morrison et al. 2011a; Chubb et al. 2013; Huang et al. 2012). Unexpectedly, the simulations produce relatively high frequencies of SLW at microphysically unstable temperatures (-20°C–0°C), although most samples were liquid-only cases whereas observations revealed more evenly dispersed frequencies of liquid-only and mixed-phase cases.

RHi CFDs reveal the high frequency of subsaturated occurrences solely corresponded with ice-only conditions. This may potentially be related to CAM5 inadequately simulating sedimentation processes into underlying subsaturated layers. This is consistent with lower averages of simulated IWC and higher averages of simulated Nc_{ice} than observed (Figure 16G–J), with the exception of slightly greater ice particle concentrations observed at temperatures >-10°C. However, this discrepancy may be related to a byproduct of the phase differentiation method. Namely, imagery from the 2DC cloud probe often captures high droplet concentrations coexisting with ice particles within mixed-phase samples. Methods for differentiating spherical and non-spherical particles exist but are associated with large uncertainties—and there is no method to determine whether droplets are liquid or frozen. In contrast, populations of small ice crystals may potentially be mistaken for droplets. Huang et al. (2017) found small ice particles having relatively high Nc_{ice} at >-9°C, consistent with secondary ice processes within shallow convective cloud fields, a common cloud regime over the Southern Ocean. However, CFDs for liquid and mixed-phase conditions are significantly supersaturated with respect to ice at temperatures as low as -30°C, further suggesting the method is capturing SLW at extremely low temperatures near that of instantaneous freezing (<-40°C).

Differences observed in the vertical profiles and gridded RHi PDFs similarly reveal greater occurrence frequencies of in-cloud subsaturated conditions. An additional notable discrepancy is seen at temperatures <-50°C, namely, CAM-collocated produces excessive cirrus (in-cloud ISS) where clear-sky ISS is observed. Due to the agreement between the datasets for RH distributions within clear-sky, liquid-only, and mixed-phase conditions, results suggest future work should focus on ice-phase processes—such as sedimentation and sublimation rates, including the treatment of ice nucleation. In addition, inclusions of the water vapor variabilities observed on the cloud scale (Diao et al. 2014) may help to increase both in-cloud ISS frequencies and magnitudes currently underestimated in CAM5 simulations at cloud fraction ranging from 0.1–0.9. Another parameter of interest is the time scale for ice crystal growth in the WBF process, which was reported to account for the majority of phase partitioning variance within MPC in CAM5 simulations (Tan and Storelvmo 2016). A potential avenue for RH evaluation may include characterizing varying time intervals of in situ observations by their spatial distribution of cloud phases. Results presented here characterize aircraft observations averaged over a given time interval as a single phase, whereas determining the heterogeneity of cloud phases can give insight into relevant cloud-scale processes. Whether cloud phases are genuinely mixed (droplets and ice particles are homogeneously mixed) or conditionally mixed (separate clusters of droplets and ice particles) will determine the significance of the interactions between liquid and ice particulates.

Chapter 4

Concluding Remarks on Small-Scale Cloud Processes and their Representation in a Weather Forecasting Model and Global Climate Model

The following studies have shown statistical analyses of RH and other cloud-relevant parameters from airborne in situ observations and compared results with simulated data from a prominent weather forecasting model (WRF; Chapter 2) and global climate model (CAM5; Chapter 3). Regions of interest include the upper troposphere during periods of strong convective activity in the midlatitudes, where the relationship between magnitudes of ISS and updraft speeds are examined (Chapter 2) and the Southern Ocean, where both the spatial distributions and magnitudes of RH as well as averaged condensed water quantities are examined at temperatures <0°C (Chapter 3).

Results from Chapter 2 reveal relatively high magnitudes of ISS observed in regions of strong convective activity, which is expected in part from the proficient vertical transport of water vapor to high altitudes as well as relatively large perturbations of vertical velocity which often result in rapid cooling rates. Simulations from WRF capture similarly high magnitudes of ISS, where some gridded data samples produce ISS near liquid saturation. However, the frequency of relatively high magnitudes of ISS (e.g., RHi>125%) in the simulations are much lower than the observations. This appears to be related to the simulated production of anomalously high number concentrations of ice particles, which act to rapidly deplete the available water vapor. Simulations predicting ice number concentrations following Cooper (1986) produce these anomalously high ice number concentrations once the simulated RHi exceeds a specified ISS threshold (e.g., RHi=108% in Morrison et al. (2005)). It was found that by increasing the specified ISS threshold to greater magnitudes of ISS (e.g., RHi=125%), frequency distributions of RHi were more comparable with observations. The simulation producing the most comparable results with observations used the Thompson and Eidhammer (2014) microphysics scheme, which is the only scheme tested that did not use the Cooper (1986) parameterization and instead uses the more recent DeMott et al. (2010) parameterization.

Results from Chapter 3 reveal relatively large occurrence frequencies of observed and simulated cloud samples containing SLW at -20°–0°C. However, the observations have higher (lower) occurrence frequencies of mixed-phase (liquid-phase) samples compared with the simulations. This trend is consistent when comparing simulations with one second observational output as well as samples averaged by 200 seconds. One second observational output is averaged over varying durations of time to produce more comparable spatial resolutions with those of CAM5. For ice phase clouds, average IWC in Obs-200s were higher by ~2 orders of magnitude (from -40°–0°C) and average Nc_{ice} were lower by ~1 order of magnitude (from -40° to -10°C) compared with the simulations, suggesting anomalously high concentrations of small ice particles are being simulated. In addition, simulations have much lower frequencies of subsaturated ice-phase samples compared with observations from -30°–0°C (Figure 19 I–K). This suggests a large frequency of sublimating ice events (ice particles falling out of clouds), an example of which is seen in Figure 13. Clear-sky ISS frequency distributions are nearly identical between the observations and simulations from -20°–0°C (e.g, Figure 18D and Figure 21A&D), suggesting that CAM5 adequately resolves low-level water vapor fields. In contrast, clear-sky ISS as well as in-cloud ISS occurrence frequencies drastically differ with decreasing temperatures <-40°C, whereby observed clear-sky ISS (in-cloud ISS) occurrence frequencies increase (decrease) with decreasing temperature (Figure 21D&E), suggesting that CAM5 is overproducing ice phase clouds in the upper troposphere. This may be in part due to the treatment of ice cloud fraction in CAM5, whereby it is diagnosed solely as a function of RHi. Expectedly, there is less variability in the occurrence frequency distributions of RHi in simulations compared with observations when results are controlled by cloud fraction (Figure 18). Thus, it is recommended that additional attention be drawn towards improving the treatment of ice cloud fraction in CAM5.

Results presented in both studies highlight the need to evaluate the treatment of cloud microphysical processes in numerical models of varying resolutions with scrutiny. Although considerable progress has been made in previous decades, large uncertainties still exist due to the difficulties associated in obtaining highly constrained and accurate observational datasets from varying observational platforms. In addition, numerical weather models often parameterize cloud scale processes based solely on satellite, radar and in situ observations irrespective of laboratory studies and even theoretical considerations. Thus, the continued validation of weather and climate models with varying observations platforms as well as theoretical considerations is necessary to further improve the representation of clouds in both weather and climate models.

References

Albrecht, B. A., 1989: Aerosols, cloud microphysics, and fractional cloudiness. *Science*, **245**, 1227–1230, doi:10.1126/science.245.4923.1227.

Ansmann, A., and Coauthors, 2008: Influence of Saharan dust on cloud glaciation in southern Morocco during the Saharan Mineral Dust Experiment. *J. Geophys. Res.*, **113**, D04210, doi:10.1029/2007JD008785. http://doi.wiley.com/10.1029/2007JD008785.

Barahona, D., and A. Nenes, 2009: Parameterizing the competition between homogeneous and heterogeneous freezing in ice cloud formation – polydisperse ice nuclei. *Atmos. Chem. Phys. Discuss.*, **9**, 10957–11004, doi:10.5194/acpd-9-10957-2009. http://www.atmos-chem-phys-discuss.net/9/10957/2009/.

Barth, M. C., and Coauthors, 2015: The Deep Convective Clouds and Chemistry (DC3) Field Campaign. *Bull. Am. Meteorol. Soc.*, **96**, 1281–1309, doi:10.1175/BAMS-D-13-00290.1.

Baumgardner, D., and Coauthors, 2017: Cloud Ice Properties: In Situ Measurement Challenges. *Meteorol. Monogr.*, **58**, 9.1-9.23, doi:10.1175/AMSMONOGRAPHS-D-16-0011.1.

Bigg, E. K., 1953: The supercooling of water. *Proc. Phys. Soc. London*, **B66**, 688–694, doi:10.1088/0370-1301/66/8/309.

Biter, C. J., J. E. Dye, D. Huffman, and W. D. King, 1987: The Drop-Size Response of the CSIRO Liquid Water Probe. *J. Atmos. Ocean. Technol.*, **4**, 359–367, doi:10.1175/1520-0426(1987)004<0359:TDSROT>2.0.CO;2.

Bodas-Salcedo, A., and Coauthors, 2014: Origins of the Solar Radiation Biases over the Southern Ocean in CFMIP2 Models*. *J. Clim.*, **27**, 41–56, doi:10.1175/JCLI-D-13-00169.1.

——, P. G. Hill, K. Furtado, K. D. Williams, P. R. Field, J. C. Manners, P. Hyder, and S. Kato, 2016: Large Contribution of Supercooled Liquid Clouds to the Solar Radiation Budget of the Southern Ocean. *J. Clim.*, **29**, 4213–4228, doi:10.1175/JCLI-D-15-0564.1.

de Boer, G., H. Morrison, M. D. Shupe, and R. Hildner, 2011: Evidence of liquid dependent ice nucleation in high-latitude stratiform clouds from surface remote sensors. *Geophys. Res. Lett.*, **38**, L01803, doi:10.1029/2010GL046016. http://doi.wiley.com/10.1029/2010GL046016.

Brown, P. R. A., and P. N. Francis, 1995: Improved Measurements of the Ice Water Content in Cirrus Using a Total-Water Probe. *J. Atmos. Ocean. Technol.*, **12**, 410–414, doi:10.1175/1520-0426(1995)012<0410:IMOTIW>2.0.CO;2.

Cesana, G., D. E. Waliser, X. Jiang, and J.-L. F. Li, 2015: Multimodel evaluation of cloud phase transition using satellite and reanalysis data. *J. Geophys. Res. Atmos.*, **120**, 7871–7892, doi:10.1002/2014JD022932.

Chen, F., and J. Dudhia, 2001: Coupling an Advanced Land Surface–Hydrology Model with the Penn State–NCAR MM5 Modeling System. Part I: Model Implementation and Sensitivity. *Mon. Weather Rev.*, **129**, 569–585, doi:10.1175/1520-0493(2001)129<0569:CAALSH>2.0.CO;2.

Chen, T., W. B. Rossow, and Y. Zhang, 2000: Radiative Effects of Cloud-Type Variations. *J.*

Clim., **13**, 264–286, doi:10.1175/1520-0442(2000)013<0264:REOCTV>2.0.CO;2.

Chubb, T. H., J. B. Jensen, S. T. Siems, and M. J. Manton, 2013: In situ observations of supercooled liquid clouds over the Southern Ocean during the HIAPER Pole-to-Pole Observation campaigns. *Geophys. Res. Lett.*, **40**, 5280–5285, doi:10.1002/grl.50986.

Cooper, W. A., 1986: Ice Initiation in Natural Clouds. *Precip. Enhanc. Sci. Challenge, Meteor. Monogr., No. 43,* Amer. Meteor. Soc., 29-32, doi:10.1007/978-1-935704-17-1_4.

D’Alessandro, J. J., and Coauthors, 2017: Dynamical conditions of ice supersaturation and ice nucleation in convective systems: A comparative analysis between in situ aircraft observations and WRF simulations. *J. Geophys. Res. Atmos.*, **122**, 2844–2866, doi:10.1002/2016JD025994.

DeMott, P. J., and Coauthors, 2010: Predicting global atmospheric ice nuclei distributions and their impacts on climate. *Proc. Natl. Acad. Sci.*, **107**, 11217–11222, doi:10.1073/pnas.0910818107.

DeMott, P. J., and Coauthors, 2011: Resurgence in Ice Nuclei Measurement Research. *Bull. Am. Meteorol. Soc.*, **92**, 1623–1635, doi:10.1175/2011BAMS3119.1. http://journals.ametsoc.org/doi/abs/10.1175/2011BAMS3119.1.

Diao, M., L. Jumbam, J. Sheffield, E. F. Wood, and M. A. Zondlo, 2013a: Validation of AIRS/AMSU-A water vapor and temperature data with in situ aircraft observations from the surface to UT/LS from 87°N-67°S. *J. Geophys. Res. Atmos.*, **118**, 6816–6836, doi:10.1002/jgrd.50483.

——, M. A. Zondlo, A. J. Heymsfield, S. P. Beaton, and D. C. Rogers, 2013b: Evolution of ice crystal regions on the microscale based on in situ observations. *Geophys. Res. Lett.*, **40**, 3473–3478, doi:10.1002/grl.50665.

——, ——, ——, L. M. Avallone, M. E. Paige, S. P. Beaton, T. Campos, and D. C. Rogers, 2014: Cloud-scale ice-supersaturated regions spatially correlate with high water vapor heterogeneities. *Atmos. Chem. Phys.*, **14**, 2639–2656, doi:10.5194/acp-14-2639-2014.

——, J. B. Jensen, L. L. Pan, C. R. Homeyer, S. Honomichl, J. F. Bresch, and A. Bansemer, 2015: Distributions of ice supersaturation and ice crystals from airborne observations in relation to upper tropospheric dynamical boundaries. *J. Geophys. Res. Atmos.*, **120**, 5101–5121, doi:10.1002/2015JD023139.

Eidhammer, T., P. J. DeMott, and S. M. Kreidenweis, 2009: A comparison of heterogeneous ice nucleation parameterizations using a parcel model framework. *J. Geophys. Res.*, **114**, D06202, doi:10.1029/2008JD011095. http://doi.wiley.com/10.1029/2008JD011095.

Ferrier, B. S., 1994: A Double-Moment Multiple-Phase Four-Class Bulk Ice Scheme. Part I: Description. *J. Atmos. Sci.*, **51**, 249–280, doi:10.1175/1520-0469(1994)051<0249:ADMMPF>2.0.CO;2.

Flatau, P. J., R. L. Walko, and W. R. Cotton, 1992: Polynomial Fits to Saturation Vapor Pressure. *J. Appl. Meteorol.*, **31**, 1507–1513, doi:10.1175/1520-0450(1992)031<1507:PFTSVP>2.0.CO;2. http://journals.ametsoc.org/doi/abs/10.1175/1520-

0450%281992%29031%3C1507%3APFTSVP%3E2.0.CO%3B2.

Frey, W. R., and J. E. Kay, 2017: The influence of extratropical cloud phase and amount feedbacks on climate sensitivity. *Clim. Dyn.*, 1–20, doi:10.1007/s00382-017-3796-5.

Gettelman, A., and S. C. Sherwood, 2016: Processes Responsible for Cloud Feedback. *Curr. Clim. Chang. Reports*, **2**, 179–189, doi:10.1007/s40641-016-0052-8.

Gettelman, A., E. J. Fetzer, A. Eldering, and F. W. Irion, 2006: The Global Distribution of Supersaturation in the Upper Troposphere from the Atmospheric Infrared Sounder. *J. Clim.*, **19**, 6089–6103, doi:10.1175/JCLI3955.1.

Gierens, K., 2003: On the transition between heterogeneous and homogeneous freezing. *Atmos. Chem. Phys.*, **3**, 437–446, doi:10.5194/acp-3-437-2003. http://www.atmos-chem-phys.net/3/437/2003/.

——, U. Schumann, M. Helten, H. Smit, and A. Marenco, 1999: A distribution law for relative humidity in the upper troposphere and lower stratosphere derived from three years of MOZAIC measurements. *Ann. Geophys.*, **17**, 1218–1226, doi:10.1007/s00585-999-1218-7.

Goff, J. A., and S. Gratch, 1946: Low-pressure properties of water from -160 to 212 F. *Trans. Am. Soc. Heat. Air-Cond. Eng.*, **52**, 95–122.

Govekar, P. D., C. Jakob, and J. Catto, 2014: The relationship between clouds and dynamics in Southern Hemisphere extratropical cyclones in the real world and a climate model. *J. Geophys. Res. Atmos.*, **119**, 6609–6628, doi:10.1002/2013JD020699. http://doi.wiley.com/10.1002/2013JD020699 (Accessed June 23, 2017).

Harrington, J. Y., M. P. Meyers, R. L. Walko, and W. R. Cotton, 1995: Parameterization of Ice Crystal Conversion Processes Due to Vapor Deposition for Mesoscale Models Using Double-Moment Basis Functions. Part I: Basic Formulation and Parcel Model Results. *J. Atmos. Sci.*, **52**, 4344–4366, doi:10.1175/1520-0469(1995)052<4344:POICCP>2.0.CO;2.

——, D. Lamb, and R. Carver, 2009: Parameterization of surface kinetic effects for bulk microphysical models: Influences on simulated cirrus dynamics and structure. *J. Geophys. Res.*, **114**, D06212, doi:10.1029/2008JD011050. http://doi.wiley.com/10.1029/2008JD011050.

Heymsfield, A. J., 1977: Precipitation Development in Stratiform Ice Clouds: A Microphysical and Dynamical Study. *J. Atmos. Sci.*, **34**, 367–381, doi:10.1175/1520-0469(1977)034<0367:PDISIC>2.0.CO;2.

——, and L. M. Miloshevich, 1995: Relative Humidity and Temperature Influences on Cirrus Formation and Evolution: Observations from Wave Clouds and FIRE II. *J. Atmos. Sci.*, **52**, 4302–4326, doi:10.1175/1520-0469(1995)052<4302:RHATIO>2.0.CO;2.

——, ——, C. Twohy, G. Sachse, and S. Oltmans, 1998: Upper-tropospheric relative humidity observations and implications for cirrus ice nucleation. *Geophys. Res. Lett.*, **25**, 1343–1346, doi:10.1029/98GL01089.

——, ——, C. Schmitt, A. Bansemer, C. Twohy, M. R. Poellot, A. Fridlind, and H. Gerber, 2005: Homogeneous Ice Nucleation in Subtropical and Tropical Convection and Its Influence on Cirrus Anvil Microphysics. *J. Atmos. Sci.*, **62**, 41–64, doi:10.1175/JAS-3360.1.

Hoskins, B. J., and K. I. Hodges, 2005: A New Perspective on Southern Hemisphere Storm Tracks. *J. Clim.*, **18**, 4108–4129, doi:10.1175/JCLI3570.1.

Huang, Y., S. T. Siems, M. J. Manton, A. Protat, and J. Delanoë, 2012: A study on the low-altitude clouds over the Southern Ocean using the DARDAR-MASK. *J. Geophys. Res. Atmos.*, **117**, doi:10.1029/2012JD017800.

——, ——, ——, G. Thompson, Y. Huang, S. T. Siems, M. J. Manton, and G. Thompson, 2014: An Evaluation of WRF Simulations of Clouds over the Southern Ocean with A-Train Observations. *Mon. Weather Rev.*, **142**, 647–667, doi:10.1175/MWR-D-13-00128.1. http://journals.ametsoc.org/doi/abs/10.1175/MWR-D-13-00128.1.

——, T. Chubb, D. Baumgardner, M. DeHoog, S. T. Siems, and M. J. Manton, 2017: Evidence for secondary ice production in Southern Ocean open cellular convection. *Q. J. R. Meteorol. Soc.*, **143**, 1685–1703, doi:10.1002/qj.3041.

Janjić, Z. I., 1994: The Step-Mountain Eta Coordinate Model: Further Developments of the Convection, Viscous Sublayer, and Turbulence Closure Schemes. *Mon. Weather Rev.*, **122**, 927–945, doi:10.1175/1520-0493(1994)122<0927:TSMECM>2.0.CO;2. http://journals.ametsoc.org/doi/abs/10.1175/1520-0493%281994%29122%3C0927%3ATSMECM%3E2.0.CO%3B2.

Jensen, E. J., and Coauthors, 2009: On the importance of small ice crystals in tropical anvil cirrus. *Atmos. Chem. Phys.*, **9**, 5519–5537, doi:10.5194/acp-9-5519-2009.

Kahn, B. H., A. Gettelman, E. J. Fetzer, A. Eldering, and C. K. Liang, 2009: Cloudy and clear-sky relative humidity in the upper troposphere observed by the A-train. *J. Geophys. Res.*, **114**, D00H02, doi:10.1029/2009JD011738.

Kärcher, B., 2012: Supersaturation Fluctuations in Cirrus Clouds Driven by Colored Noise. *J. Atmos. Sci.*, **69**, 435–443, doi:10.1175/JAS-D-11-0151.1. http://journals.ametsoc.org/doi/abs/10.1175/JAS-D-11-0151.1.

——, and W. Haag, 2004: Factors controlling upper tropospheric relative humidity. *Ann. Geophys.*, **22**, 705–715, doi:10.5194/angeo-22-705-2004.

Kay, J. E., and Coauthors, 2012: Exposing Global Cloud Biases in the Community Atmosphere Model (CAM) Using Satellite Observations and Their Corresponding Instrument Simulators. *J. Clim.*, **25**, 5190–5207, doi:10.1175/JCLI-D-11-00469.1.

Kay, J. E., C. Wall, V. Yettella, B. Medeiros, C. Hannay, P. Caldwell, and C. Bitz, 2016: Global Climate Impacts of Fixing the Southern Ocean Shortwave Radiation Bias in the Community Earth System Model (CESM). *J. Clim.*, **29**, 4617–4636, doi:10.1175/JCLI-D-15-0358.1.

King, W. D., D. A. Parkin, and R. J. Handsworth, 1978: A Hot-Wire Liquid Water Device Having Fully Calculable Response Characteristics. *J. Appl. Meteorol.*, **17**, 1809–1813, doi:10.1175/1520-0450(1978)017<1809:AHWLWD>2.0.CO;2.

Komurcu, M., and Coauthors, 2014: Intercomparison of the cloud water phase among global climate models. *J. Geophys. Res. Atmos.*, **119**, 3372–3400, doi:10.1002/2013JD021119.

Koop, T., B. Luo, A. Tsias, and T. Peter, 2000a: Water activity as the determinant for homogeneous ice nucleation in aqueous solutions. *Nature*, **406**, 611–614, doi:10.1038/35020537.

Koop, T., B. Luo, A. Tsias, and T. Peter, 2000b: Water activity as the determinant for homogeneous ice nucleation in aqueous solutions. *Nature*, **406**, 611–614, doi:10.1038/35020537.

Korolev, A., and Coauthors, 2017: Mixed-Phase Clouds: Progress and Challenges. *Meteorol. Monogr.*, **58**, 5.1-5.50, doi:10.1175/AMSMONOGRAPHS-D-17-0001.1.

Korolev, A. V., and I. P. Mazin, 2003: Supersaturation of Water Vapor in Clouds. *J. Atmos. Sci.*, **60**, 2957–2974, doi:10.1175/1520-0469(2003)060<2957:SOWVIC>2.0.CO;2.

——, and G. A. Isaac, 2006: Relative Humidity in Liquid, Mixed-Phase, and Ice Clouds. *J. Atmos. Sci.*, **63**, 2865–2880, doi:10.1175/JAS3784.1.

——, ——, S. G. Cober, J. W. Strapp, and J. Hallett, 2003: Microphysical characterization of mixed-phase clouds. *Q. J. R. Meteorol. Soc.*, **129**, 39–65, doi:10.1256/qj.01.204.

——, E. Emery, and K. Creelman, 2013a: Modification and Tests of Particle Probe Tips to Mitigate Effects of Ice Shattering. *J. Atmos. Ocean. Technol.*, **30**, 690–708, doi:10.1175/JTECH-D-12-00142.1.

——, E. F. Emery, J. W. Strapp, S. G. Cober, and G. A. Isaac, 2013b: Quantification of the Effects of Shattering on Airborne Ice Particle Measurements. *J. Atmos. Ocean. Technol.*, **30**, 2527–2553, doi:10.1175/JTECH-D-13-00115.1.

Krämer, M., and Coauthors, 2009: Ice supersaturations and cirrus cloud crystal numbers. *Atmos. Chem. Phys.*, **9**, 3505–3522, doi:10.5194/acp-9-3505-2009.

Krämer, M., and Coauthors, 2016: A microphysics guide to cirrus clouds – Part 1: Cirrus types. *Atmos. Chem. Phys.*, **16**, 3463–3483, doi:10.5194/acp-16-3463-2016.

Lamquin, N., C. J. Stubenrauch, K. Gierens, U. Burkhardt, and H. Smit, 2012: A global climatology of upper-tropospheric ice supersaturation occurrence inferred from the Atmospheric Infrared Sounder calibrated by MOZAIC. *Atmos. Chem. Phys.*, **12**, 381–405, doi:10.5194/acp-12-381-2012.

Lawson, R. P., and A. Gettelman, 2014: Impact of Antarctic mixed-phase clouds on climate. *Proc. Natl. Acad. Sci. U. S. A.*, **111**, 18156–18161, doi:10.1073/pnas.1418197111. http://www.ncbi.nlm.nih.gov/pubmed/25489069 (Accessed June 23, 2017).

Li, J.-L. F., D. E. Waliser, G. Stephens, S. Lee, T. L'Ecuyer, S. Kato, N. Loeb, and H.-Y. Ma, 2013: Characterizing and understanding radiation budget biases in CMIP3/CMIP5 GCMs, contemporary GCM, and reanalysis. *J. Geophys. Res. Atmos.*, **118**, 8166–8184, doi:10.1002/jgrd.50378.

Li, Z.-X., and H. Le Treut, 1992: Cloud-radiation feedbacks in a general circulation model and their dependence on cloud modelling assumptions. *Clim. Dyn.*, **7**, 133–139, doi:10.1007/BF00211155.

Liou, K.-N., 1986: Influence of Cirrus Clouds on Weather and Climate Processes: A Global Perspective. *Mon. Weather Rev.*, **114**, 1167–1199, doi:10.1175/1520-0493(1986)114<1167:IOCCOW>2.0.CO;2.

Mace, G. G., R. Marchand, Q. Zhang, and G. Stephens, 2007: Global hydrometeor occurrence as observed by CloudSat: Initial observations from summer 2006. *Geophys. Res. Lett.*, **34**, doi:10.1029/2006GL029017. http://doi.wiley.com/10.1029/2006GL029017 (Accessed March 15, 2018).

McCoy, D. T., D. L. Hartmann, and D. P. Grosvenor, 2014: Observed Southern Ocean Cloud Properties and Shortwave Reflection. Part II: Phase Changes and Low Cloud Feedback*. *J. Clim.*, **27**, 8858–8868, doi:10.1175/JCLI-D-14-00288.1.

Mitchell, J. F. B., C. A. Senior, and W. J. Ingram, 1989: C02 and climate: a missing feedback? *Nature*, **341**, 132–134, doi:10.1038/341132a0.

Mlawer, E. J., S. J. Taubman, P. D. Brown, M. J. Iacono, and S. A. Clough, 1997: Radiative transfer for inhomogeneous atmospheres: RRTM, a validated correlated-k model for the longwave. *J. Geophys. Res. Atmos.*, **102**, 16663–16682, doi:10.1029/97JD00237. http://doi.wiley.com/10.1029/97JD00237.

Morrison, A. E., S. T. Siems, and M. J. Manton, 2011a: A Three-Year Climatology of Cloud-Top Phase over the Southern Ocean and North Pacific. *J. Clim.*, **24**, 2405–2418, doi:10.1175/2010JCLI3842.1.

Morrison, H., and J. O. Pinto, 2006: Intercomparison of Bulk Cloud Microphysics Schemes in Mesoscale Simulations of Springtime Arctic Mixed-Phase Stratiform Clouds. *Mon. Weather Rev.*, **134**, 1880–1900, doi:10.1175/MWR3154.1.

Morrison, H., and A. Gettelman, 2008: A New Two-Moment Bulk Stratiform Cloud Microphysics Scheme in the Community Atmosphere Model, Version 3 (CAM3). Part I: Description and Numerical Tests. *J. Clim.*, **21**, 3642–3659, doi:10.1175/2008JCLI2105.1.

Morrison, H., J. A. Curry, and V. I. Khvorostyanov, 2005: A New Double-Moment Microphysics Parameterization for Application in Cloud and Climate Models. Part I: Description. *J. Atmos. Sci.*, **62**, 1665–1677, doi:10.1175/JAS3446.1.

——, G. Thompson, and V. Tatarskii, 2009: Impact of Cloud Microphysics on the Development of Trailing Stratiform Precipitation in a Simulated Squall Line: Comparison of One- and Two-Moment Schemes. *Mon. Weather Rev.*, **137**, 991–1007, doi:10.1175/2008MWR2556.1.

Morrison, H., G. de Boer, G. Feingold, J. Harrington, M. D. Shupe, and K. Sulia, 2011b: Resilience of persistent Arctic mixed-phase clouds. *Nat. Geosci.*, **5**, 11–17, doi:10.1038/ngeo1332.

Muhlbauer, A., T. P. Ackerman, J. M. Comstock, G. S. Diskin, S. M. Evans, R. P. Lawson, and R. T. Marchand, 2014: Impact of large-scale dynamics on the microphysical properties of midlatitude cirrus. *J. Geophys. Res. Atmos.*, **119**, 3976–3996, doi:10.1002/2013JD020035.

Murphy, D. M., and T. Koop, 2005: Review of the vapour pressures of ice and supercooled water for atmospheric applications. *Q. J. R. Meteorol. Soc.*, **131**, 1539–1565, doi:10.1256/qj.04.94.

Ovarlez, H., K. Gierens, and J. Stro, 2002a: Water vapour measurements inside cirrus clouds in Northern and Southern hemispheres during INCA. **29**, 2–5.

Ovarlez, J., J.-F. Gayet, K. Gierens, J. Ström, H. Ovarlez, F. Auriol, R. Busen, and U. Schumann, 2002b: Water vapour measurements inside cirrus clouds in Northern and Southern hemispheres during INCA. *Geophys. Res. Lett.*, **29**, 60-1-60–64, doi:10.1029/2001GL014440.

Peter, T., C. Marcolli, P. Spichtinger, T. Corti, M. B. Baker, and T. Koop, 2006: When dry air is too humid. *Science*, **314**, 1399–1402, doi:10.1126/science.1135199.

Phillips, V. T. J., P. J. DeMott, C. Andronache, V. T. J. Phillips, P. J. DeMott, and C. Andronache, 2008: An Empirical Parameterization of Heterogeneous Ice Nucleation for Multiple Chemical Species of Aerosol. *J. Atmos. Sci.*, **65**, 2757–2783, doi:10.1175/2007JAS2546.1.

Pruppacher, H. R., and J. D. Klett, 1996: *Microphysics of Clouds and Precipitation*. Springer Netherlands,.

Reisner, J., R. M. Rasmussen, and R. T. Bruintjes, 1998: Explicit forecasting of supercooled liquid water in winter storms using the MM5 mesoscale model. *Q. J. R. Meteorol. Soc.*, **124**, 1071–1107, doi:10.1002/qj.49712454804.

Sheridan, L. M., J. Y. Harrington, D. Lamb, K. Sulia, L. M. Sheridan, J. Y. Harrington, D. Lamb, and K. Sulia, 2009: Influence of ice crystal aspect ratio on the evolution of ice size spectra during vapor depositional growth. *J. Atmos. Sci.*, **66**, 3732–3743, doi:10.1175/2009JAS3113.1.

Solomon, A., M. D. Shupe, P. O. G. Persson, and H. Morrison, 2011: Moisture and dynamical interactions maintaining decoupled Arctic mixed-phase stratocumulus in the presence of a humidity inversion. *Atmos. Chem. Phys.*, **11**, 10127–10148, doi:10.5194/acp-11-10127-2011.

Spichtinger, P., K. Gierens, U. Leiterer, and H. Dier, 2003a: Ice supersaturation in the tropopause region over Lindenberg, Germany. *Meteorol. Zeitschrift*, **12**, 143–156, doi:10.1127/0941-2948/2003/0012-0143.

——, ——, and W. Read, 2003b: The global distribution of ice-supersaturated regions as seen by the Microwave Limb Sounder. *Q. J. R. Meteorol. Soc.*, **129**, 3391–3410, doi:10.1256/qj.02.141.

Spichtinger, P., K. Gierens, and A. Dörnbrack, 2005a: Formation of ice supersaturation by mesoscale gravity waves. *Atmos. Chem. Phys.*, **5**, 1243–1255, doi:10.5194/acp-5-1243-2005.

——, ——, and H. Wernli, 2005b: A case study on the formation and evolution of ice supersaturation in the vicinity of a warm conveyor belt's outflow region. *Atmos. Chem. Phys.*, **5**, 973–987.

Srivastava, R. C., and J. L. Coen, 1992: New Explicit Equations for the Accurate Calculation of the Growth and Evaporation of Hydrometeors by the Diffusion of Water Vapor. *J. Atmos. Sci.*, **49**, 1643–1651, doi:10.1175/1520-0469(1992)049<1643:NEEFTA>2.0.CO;2.

Stephens, B. B., and Coauthors, 2018: The O 2 /N 2 Ratio and CO 2 Airborne Southern Ocean Study. *Bull. Am. Meteorol. Soc.*, **99**, 381–402, doi:10.1175/BAMS-D-16-0206.1.

Stocker, T. F., and Coauthors, 2013: *IPCC, 2013: Climate Change 2013 - The Physical Science Basis. Contribution of Working Group I to the Fifth Assessment Report of the Intergovernmental Panel on Climate Change*. Intergovernmental Panel on Climate Change, Ed. Cambridge University Press, Cambridge,.

Stubenrauch, C. J., S. Cros, A. Guignard, and N. Lamquin, 2010: A 6-year global cloud climatology from the Atmospheric InfraRed Sounder AIRS and a statistical analysis in synergy with CALIPSO and CloudSat. *Atmos. Chem. Phys.*, **10**, 7197–7214, doi:10.5194/acp-10-7197-2010. http://www.atmos-chem-phys.net/10/7197/2010/ (Accessed March 15, 2018).

Sun, Z., and K. P. Shine, 1994: Studies of the radiative properties of ice and mixed-phase clouds. *Q. J. R. Meteorol. Soc.*, **120**, 111–137, doi:10.1002/qj.49712051508. http://doi.wiley.com/10.1002/qj.49712051508.

Tan, I., and T. Storelvmo, 2016: Sensitivity Study on the Influence of Cloud Microphysical Parameters on Mixed-Phase Cloud Thermodynamic Phase Partitioning in CAM5. *J. Atmos. Sci.*, **73**, 709–728, doi:10.1175/JAS-D-15-0152.1.

——, ——, and M. D. Zelinka, 2016: Observational constraints on mixed-phase clouds imply higher climate sensitivity. *Science*, **352**, 224–227, doi:10.1126/science.aad5300.

Thompson, G., and T. Eidhammer, 2014: A Study of Aerosol Impacts on Clouds and Precipitation Development in a Large Winter Cyclone. *J. Atmos. Sci.*, **71**, 3636–3658, doi:10.1175/JAS-D-13-0305.1.

——, P. R. Field, R. M. Rasmussen, and W. D. Hall, 2008: Explicit Forecasts of Winter Precipitation Using an Improved Bulk Microphysics Scheme. Part II: Implementation of a New Snow Parameterization. *Mon. Weather Rev.*, **136**, 5095–5115, doi:10.1175/2008MWR2387.1.

Trenberth, K. E., and J. T. Fasullo, 2010: Simulation of Present-Day and Twenty-First-Century Energy Budgets of the Southern Oceans. *J. Clim.*, **23**, 440–454, doi:10.1175/2009JCLI3152.1.

Twomey, S., 1977: The Influence of Pollution on the Shortwave Albedo of Clouds. *J. Atmos. Sci.*, **34**, 1149–1152, doi:10.1175/1520-0469(1977)034<1149:TIOPOT>2.0.CO;2.

Vidaurre, G., J. Hallett, D. C. Rogers, G. Vidaurre, J. Hallett, and D. C. Rogers, 2011: Airborne Measurement of Liquid and Total Water Content. *J. Atmos. Ocean. Technol.*, **28**, 1088–1103, doi:10.1175/JTECH-D-10-05035.1.

Wu, C., X. Liu, M. Diao, K. Zhang, A. Gettelman, Z. Lu, J. E. Penner, and Z. Lin, 2017: Direct comparisons of ice cloud macro- and microphysical properties simulated by the Community Atmosphere Model version 5 with HIPPO aircraft observations. *Atmos. Chem. Phys.*, **17**, 4731–4749, doi:10.5194/acp-17-4731-2017.

Wylie, D. P., and W. P. Menzel, 1999: Eight Years of High Cloud Statistics Using HIRS. *J. Clim.*, **12**, 170–184, doi:10.1175/1520-0442(1999)012<0170:EYOHCS>2.0.CO;2.

Zhang, C., and J. Y. Harrington, 2015: The Effects of Surface Kinetics on Crystal Growth and Homogeneous Freezing in Parcel Simulations of Cirrus. *J. Atmos. Sci.*, **72**, 2929–2946, doi:10.1175/JAS-D-14-0285.1. http://journals.ametsoc.org/doi/10.1175/JAS-D-14-0285.1.

Zondlo, M. A., M. E. Paige, S. M. Massick, and J. A. Silver, 2010: Vertical cavity laser hygrometer for the National Science Foundation Gulfstream-V aircraft. *J. Geophys. Res.*, **115**, D20309, doi:10.1029/2010JD014445.